NONLINEAR ULTRASONIC TECHNIQUE FOR THE CHARACTERIZATION OF MICROSTRUCTURE IN ADDITIVE MATERIALS

A Dissertation
Presented to
The Academic Faculty

by

Aurelio Bellotti

In Partial Fulfillment
of the Requirements for the Degree
Master of Science in the
G.W. Woodruff School of Mechanical Engineering

Georgia Institute of Technology
August 2020

NONLINEAR ULTRASONIC TECHNIQUE FOR THE CHARACTERIATION OF MICROSTRUCTURE IN ADDITIVE MATERIALS

Approved by:

Dr. Laurence Jacobs, Advisor
School of Mechanical Engineering
Georgia Institute of Technology

Dr. Jin-Yeon Kim
School of Civil Engineering
Georgia Institute of Technology

Dr. Christopher Saldana
School of Mechanical Engineering
Georgia Institute of Technology

Date Approved: June 25, 2020

ACKNOWLEDGEMENTS

I would first like to thank my advisors, Dr. Laurence Jacobs and Dr. Jin-Yeon Kim. I chose to attend Georgia Tech based on their work and recommendations of their excellent advising. These recommendations have proven to be true, as both have tremendously helped me understand not only the technical content, but also how to be an effective researcher. I would also like to thank Dr. Chris Saldana for carving out time during a hectic period to be a member of my committee.

I would like to thank Sandia National Labs for providing financial support and materials at the beginning of this thesis work. The materials and time provided by Sandia gave a ground truth to this project, and for that I am thankful. Dr. Joe Bishop, Dr. Bradley Jared, Dr. Kyle Johnson, Dr. Don Susan and Philip Noel, all from Sandia, have been excellent collaborators throughout this research project. They have provided their individual expertise and were also great hosts.

I would like to thank the NEUP for providing me with financial support through the University Program Graduate Fellowship, which has funded me during the completion of this work and will help fund me through the completion of my PhD.

I would like to thank all my lab mates I have had the pleasure to work with. This includes two undergraduate students, Vivek Garimella and Gregor Wettermann, whose questioning helped solidify my fundamentals on the topic. I would like to thank the wonderful group of lab mates including Kathrin Hoffmann, Sangyun Park, Denis Pfeifer, Niklas Fahse, Marius Goletz, Max May, Denis Smajic and Hengyu Yang. They have been

great colleagues and friends during our time in lab and across the country attending conferences. I would like to particularly thank Brian Fuchs and Katie Scott Levy who taught me how to make measurements, about grad school, with course work, during Qualifying exams, and for their friendship.

I would like to thank my family who have always been there for me with their love and encouragement. My parents have always emphasized the importance of education, which has led to my pursuit of graduate degrees. My brothers have been great examples for me to follow and are always a great source of guidance. I would like to thank Brinkley Raynor for her help and support throughout graduate school.

TABLE OF CONTENTS

LIST OF TABLES

LIST OF FIGURES

LIST OF SYMBOLS AND ABBREVIATIONS

AM	Additive Manufacturing
NDE	Nondestructive evaluation
NLU	Nonlinear Ultrasound
SHG	Second Harmonic Generation
β	Acoustic Nonlinearity Parameter
GNDs	Geometrically Necessary Dislocations
EBSD	Electron Backscatter Diffraction
ρ	Density, t is time, σ is the Cauchy stress tensor,
t	Time
σ	Cauchy Stress Tensor
u	Particle Displacement
x^*	Eulerian Coordinate
F	Deformation Gradient Tensor
E	Lagrangian Strain Tensor
P	First Piola-Kirchoff Stress Tensor
ρ_o	Undeformed Body Density
∇_x	Gradient in Lagrangian Coordinates
W	Specific Strain Energy per Mass
C_{ijkl}	Second Order Moduli
C_{ijklmn}	Third Order Moduli
O	Higher Order Terms
δ_{ij}	Kroneckor Delta

A_2^e, A_3^e	Huang Coefficients
A	Wave Amplitude
ω	Angular Frequency
k	Wavenumber
c_L	Longitudinal Wave Speed
k_R	Rayleigh Wavenumber
k_L	Longitudinal Wavenumber
k_S	Shear Wavenumber
A_1	Fundamental Frequency Amplitude
A_2	Second Harmonic Amplitude
L	Half Dislocation Distance
r	Arc Radius
θ	Arc Angle
τ	Shear Stress
m	Schmid Factor
ϕ	Angle of Vector Normal to Glide Plane
λ	Glide Direction
T	Line Tension
b	Burger's Vector
G	Shear Modulus
γ	Shear Strain
Λ	Dislocation Density
S	Area Swept by Dislocation Segment
Ω	Conversion of Shear strain to Longitudinal
E_1	Second Order Elastic Constants

E_2	Third Order Elastic Constants
$\alpha_a(f)$	Absorption Attenuation Coefficient
$\alpha_s(f)$	Scattering Attenuation Coefficient
f	Frequency
z	Sample Thickness
λ	Wavelength
D	Complex Diffraction Correction Function
J_n	Bessel Function of the First Kind of Order n
v	Measured Voltage
SNR	Signal-to-Noise Ratio
ROD	Reference Orientation Deviation

SUMMARY

This thesis employs nonlinear ultrasonic techniques to track microstructural changes in additively manufactured (AM) metals. Adoption of AM in critical scenarios has been slowed by uncertainty stemming from variations in the resultant piece. Different print iterations of the same part could have varying mechanical properties dependent on printing parameters. High temperature gradients created during the printing process can lead to increased dislocation density. Non-destructive evaluation could be used to quantify the dislocation density within a printed part. This information could be used in a multi-physics certification of AM parts before they are used in critical scenarios.

Second harmonic generation techniques based on the transmission of Rayleigh surface waves are used to measure the acoustic nonlinearity parameter, β. Stainless steel specimens are made through three procedures: traditional wrought manufacturing; powder bed fusion (PBF); and laser engineered net shaping (LENS). The β parameter is measured through successive steps of an annealing heat treatment intended to decrease dislocation density.

In agreement with fundamental material models for the dislocation-acoustic nonlinearity relationship second harmonic generation, β is shown to drop in each sample throughout the heat treatment before recrystallization. Geometrically necessary dislocations (GND) are measured from electron back scatter diffraction (EBSD) as a quantitative indicator of dislocations. Average GND density and β are found to have a statistical correlation coefficient of 0.852 showing sensitivity of β to dislocations in AM metals.

CHAPTER 1. INTRODUCTION

1.1 Motivation

Additive manufacturing (AM) allows for the rapid creation of complex parts that would be difficult to achieve through traditional subtractive manufacturing methods. Internal geometries can be made to have material properties tailored for specific use cases [1]. A variety of materials can be used in AM, including stainless steels that are commonly employed in mission critical components for the energy, defense, and aerospace industries. Concerns about the qualification procedure of AM parts has delayed the adoption of AM in these consequential industries [2]. Qualification challenges include novel material modeling problems [3,4] and variation in the manufacturing process [5].

Manufacturing variables (e.g., laser scanning velocity, powder deposition rate, timing between layers, laser power) can change the thermal history of a part [5]. Large thermal gradients are generated between the local melt pool and the remaining structure [4]. Heterogeneous thermal expansion resulting from these thermal gradients can create high local stresses leading to the formation of plastic strains and distortions [4]. Distortions of the crystal lattice are resolved by the creation of dislocations [6,7]. The mechanical performance of a part is strongly dependent on its microstructure including grain structures, dislocations, porosity, and residual stresses [8].

Mechanical testing can give information on material parameters, but at the cost of physically altering the part. Inconsistencies in printing variables can cause microstructural changes that alter the mechanical properties between print iterations [5]. Nondestructive

evaluation (NDE) could be used as a comparative tool to analyze the microstructures from different print iterations, helping to validate an AM part before its use in critical scenarios. In addition, any new microstructural data obtained from NDE can be integrated into a qualification procedure for AM. This work proposes the use of nonlinear ultrasound (NLU) as a quantitative measure to track changes in the microstructure of AM metals. Second harmonic generation (SHG) is the measurement technique used in this work.

1.2 Previous Works of NDE for AM

Previous efforts to integrate NDE into the qualification and validation of AM have been made [2]. Inadequacies of these previous efforts include lack of in-situ measurements for real-time process control, inability to implement changes to AM system due to warranty requirements, and the wide variance in microstructure [9]. NDE techniques previously used include computed tomography, eddy current testing, x-ray digital radiographic testing, linear ultrasound, and near infrared camera inspection to assess melt pool temperatures [2]. Five areas of inadequacies in NDE for AM were identified by NASA as [2]:

1. Material Input: the need of NDE to characterize the materials inputted into the AM process, particularly bulk powder properties.
2. Finished Part: using NDE to investigate finished parts include before and after post-processing. These investigations would help understand the flaws produced in the AM process and their effects.
3. Effects of Defects: NDE can be used to characterize defect type, frequency and size and help in the understanding of these on performance.

4. Design Allowables Database: the effects of process variables can be investigated with NDE
5. Physical Reference Standards: a database of physical standards/data can be created for calibration and standardization of NDE techniques

The research presented in this thesis seeks to answer areas 2 and 3.

1.3 Objectives

This thesis explores the sensitivity of the acoustic nonlinearity parameter, β to the microstructural features in AM parts. It relates changes in the measured β to decreases in the dislocation density that are approximated by geometrically necessary dislocations (GNDs) that are independently measured with electron backscatter diffraction (EBSD).

A post-AM heat treatment plan is used to force a change in the material microstructure, i.e. the reduction of the dislocation density. The β parameter is measured through successive steps of this annealing heat treatment, while complementary linear ultrasound, hardness, and EBSD measurements are used to provide independent evidence of microstructural changes. Specimens for hardness and EBSD are cut from the "parent" samples with each successive stage of heat treatment.

1.4 Structure of Thesis

Overviews of Nonlinear Ultrasound, Second Harmonic Generation, and Rayleigh Waves are first presented in Chapter 2. With this foundation, derivations of the Nonlinear Wave Parameter can be made in general and for the intended measurement setup. A basic model describing the potential microstructural contributions to ultrasonic nonlinearity is

then presented. A linear acoustic parameter, attenuation, is also introduced and the relative coefficient of attenuation is derived at the end of Chapter 2.

Chapter 3 details the specimens used in this study including the differences in material composition and manufacturing techniques. Background on the two AM techniques used in this study are provided. The annealing heat treatment plan, specimen preparations and the proposed effects are described.

Chapter 4 provides a thorough description of the experimental procedures used for each measurement (Rayleigh Wave, NLU, Vickers Microhardness, EBSD and resultant GND estimations, and Acoustic Attenuation).

Chapter 5 introduces the results for each measurement separately. The results before complete recrystallization are introduced first and the potential meaning of the changes observed are discussed. Under Section 5.7, each subsection updates the results given at the beginning of Chapter 5 with the data containing recrystallized results.

Chapter 6 concludes the thesis with an overview of the work and a recap of the discussions made from the results. Future works for NDE of AM materials and specific continuations of the work in this thesis are given.

CHAPTER 2. THEORY

2.1 Nonlinear Ultrasound Overview

This thesis determines the sensitivity of nonlinear ultrasound (NLU) to microstructural changes in AM metals. NLU is a category of NDE techniques based on the detection of different harmonics generated from an input consisting of a single frequency ultrasonic wave. Distortion of the inputted wave occur from its interaction with microstructural features. By quantifying this distortion, NLU can be used to compare microstructural features across different specimens, materials, and material states. NLU measurements are sensitive damage much smaller than the inputted wavelength [8]. Restrictions to the input wavelength size may come from depth penetration requirements and measurement equipment limitations. By investigating features orders of magnitude smaller than the input wavelength, NLU can give precursor information prior to material failure and can be used to characterize microstructure in ways that are impossible with linear ultrasonic techniques.

NLU shares many of the same benefits as conventional linear ultrasonic methods. Both can be used to evaluate surface and sub-surface material. They are both capable of providing valuable material information at a lower cost compared to some other NDE methods [10]. Both can be performed with only single-sided access which is beneficial when testing hazardous material containers including pipelines and reactor.

2.2 Second Harmonic Generation Overview

Second harmonic generation (SHG) is a subset measurement technique under NLU that uses the inherent nonlinear stress-strain relationship of a material. A linear ultrasonic

wave travels through a material and distorts in relation to the amount of nonlinearity extant in the material. The acoustic energy at the fundamental frequency of the input ultrasonic wave is transferred to higher harmonics [11]. The decrease of energy of the fundamental frequency and increase to the second harmonic are measurable and are quantified with the acoustic nonlinearity parameter, β, whose derivation will be presented in Section 2.4. β is an absolute material property, but the relative changes to β will be used for ease of measurement. This parameter can give indication to the amount of nonlinearity in a material and is sensitive to specific microstructural features as detailed in Section 2.5. As such, β is used as the quantitative measure for microstructural changes in the AM metals studied in this work.

2.2.1 Previous Work: Second Harmonic Generation (SHG)

SHG has been previously demonstrated to detect microstructural changes including dislocation formation during fatigue [12], precipitate formation [13], and thermal aging [14]. SHG techniques have previously shown to be sensitive to changes in dislocation density [11], but their use in the qualification of AM materials has not been fully explored.

2.3 Rayleigh Wave Overview

SHG will be quantified through a Rayleigh wave measurement setup that is detailed in Section 4.1. Rayleigh waves are surface acoustic waves that propagate along the free surface of an elastic half-space [15]. Rayleigh wave motion is limited to a layer of approximately one wavelength below the surface and rapidly decays through the depth. Rayleigh wave motion includes both transverse and longitudinal components that is manifested in a retrograde elliptical particle motion, seen in Figure 1.

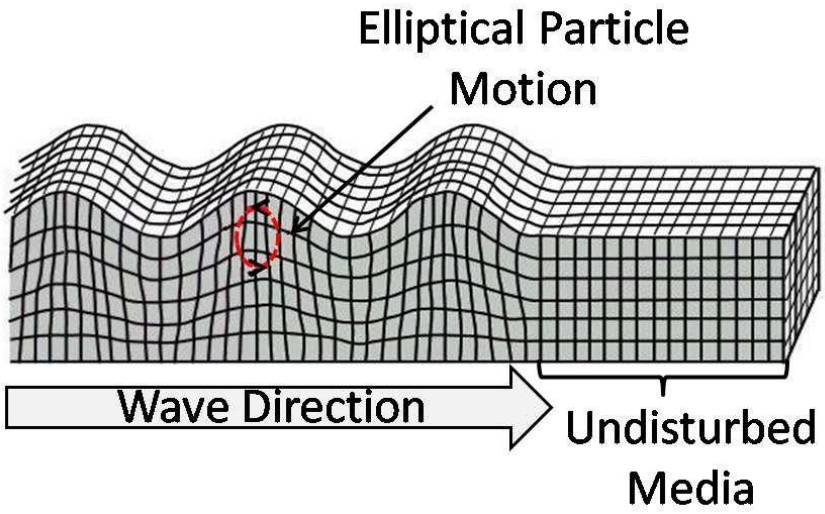

Figure 1: Rayleigh wave motion [16]

2.4 Nonlinear Wave Propagation

2.4.1 Derivation of Nonlinearity Parameter

Consider a single frequency sinusoidal longitudinal wave propagating in an isotropic material with quadratic nonlinearity [11]. The assumption of an isotropic material for the application of AM will be discussed in Section 3.1.3. Following the derivation of Hamilton and Blackstock [17], the one-dimension equation of motion is given by:

$$\rho \frac{\partial^2 \boldsymbol{u}}{\partial t^2} = \nabla \cdot \boldsymbol{\sigma} \tag{1}$$

where ρ is density, t is time, σ is the Cauchy stress tensor, and $(\nabla \cdot \boldsymbol{\sigma})_i = \partial \sigma_{ij} / \partial \mathrm{x}_j$, with summation over repeated indices implied. u is particle displacement from an initial point in Lagrangian coordinates ($\boldsymbol{x}$) to the same point in Eulerian coordinates ($\boldsymbol{x}^*$) and is defined as $\boldsymbol{u}=\boldsymbol{x}^*-\boldsymbol{x}$.

Equation 1 is expressed in a Eulerian, or spatial, coordinates; typically, nonlinear elasticity in solids is presented in Lagrangian, or material coordinates. The deformation gradient tensor relates the spatial and material frames:

$$\boldsymbol{F} = \frac{\partial \boldsymbol{x}^*}{\partial \boldsymbol{x}} \tag{2}$$

From this, the Lagrangian strain tensor is defined as:

$$\begin{gathered} \boldsymbol{E} = \frac{1}{2}(\boldsymbol{F}^T \cdot \boldsymbol{F} - I) \\ E_{ij} = \frac{1}{2}\left(\frac{\partial u_i}{\partial x_j} + \frac{\partial u_j}{\partial x_i} + \frac{\partial u_k}{\partial x_i} + \frac{\partial u_k}{\partial x_j}\right) \end{gathered} \tag{3}$$

in both matrix and indices notations. The first Piola-Kirchoff stress tensor is introduced:

$$\boldsymbol{P} = \frac{\rho_o}{\rho}\boldsymbol{\sigma} \cdot \boldsymbol{F}^{-T} \tag{4}$$

where, in Lagrangian coordinates, ρ_o and ρ are the densities of the undeformed and deformed bodies, respectively. Substitution of the Piola-Kirchoff stress tensor Equation 4 into the Eulerian equation of motion (Equation 1) and use of the Euler-Piola-Jacobi identity provides the equation of motion in Lagrangian coordinates without body forces:

$$\rho_0 \frac{\partial^2 \boldsymbol{u}}{\partial t^2} = \nabla_x \cdot \boldsymbol{P} \tag{5}$$

where ∇_x is the gradient in the Lagrangian coordinates. The specific strain energy per mass W is a function of local deformation volume changes and is therefore a function of the Lagrangian strain tensor $\boldsymbol{E}$. The Piola-Kirchoff stress tensor can then be rewritten as:

$$\boldsymbol{P} = \rho_0 \boldsymbol{F} \cdot \frac{\partial W}{\partial \boldsymbol{E}} \tag{6}$$

A Taylor expansion for small but not negligible strain leads to the following:

$$\rho_0 W = \frac{1}{2!} C_{ijkl} E_{ij} E_{kl} + \frac{1}{3!} C_{ijklmn} E_{ij} E_{kl} E_{mn} + O \tag{7}$$

where C_{ijkl} and C_{ijklmn} are the second and third order elastic moduli, respectively, and O are higher order terms that are neglected with the assumption of small strain. This allows the Piola-Kirchoff stress tensor in Equation 6 to be rewritten as:

$$P_{ij} = C_{ijkl} \frac{\partial u_k}{\partial x_l} + \frac{1}{2} M_{ijklmn} \frac{\partial u_k}{\partial x_l} \frac{\partial u_m}{\partial x_n} + \frac{1}{3} M_{ijklmn} \frac{\partial u_k}{\partial x_l} \frac{\partial u_m}{\partial x_n} \frac{\partial u_p}{\partial x_q} + \cdots \tag{8}$$

With the higher order tensor being defined as:

$$M_{ijklmn} = C_{ijklmn} + C_{ijkln}\delta_{km} + C_{jnkl}\delta_{im} + C_{jlmn}\delta_{ik} \tag{9}$$

where δ_{ij} is the Kronecker delta. Substitution of Equations 8 and 8988 into Equation 5 gives the nonlinear wave equation:

$$\frac{\partial^2 u_i}{\partial t^2} = \frac{1}{\rho_0} \frac{\partial^2 u_k}{\partial x_j \partial x_l} \left(C_{ijkl} + M_{ijklmn} \frac{\partial u_m}{\partial x_n} \right) \tag{10}$$

The second and third order elastic constants of M_{ijklmn} in Equation 10 can be expressed using Voigt notation $(C_{ijklmn} = C_{IJK})$, then one-dimensional wave motion in one direction is written:

$$\frac{\partial^2 u_1}{\partial t^2} = \frac{1}{\rho_0}\frac{\partial^2 u_1}{\partial {x_1}^2}\left(C_{11} + (C_{1111} + 3C_{11})\frac{\partial u_1}{\partial x_1}\right) \tag{11}$$

Alternatively, the Huang coefficients $(A_2^e = C_1 + C_{11};\ A_3^e = C_{111} + 3C_{11})$ are substituted into Equation 11:

$$\frac{\partial^2 u_1}{\partial t^2} = \frac{1}{\rho_0}\frac{\partial^2 u_1}{\partial {x_1}^2}A_2^e\left(1 + \frac{A_3^e}{A_2^e}\frac{\partial u_1}{\partial x_1}\right) \tag{12}$$

where the ratio of Huang coefficients is defined as the acoustic nonlinearity parameter [12].

$$\beta = \frac{A_3^e}{A_2^e} = \frac{C_{111} + 3C_{11}}{C_1 + C_{11}} \tag{13}$$

Consider an excitation of a harmonic wave of amplitude *A* and frequency *ω:*

$$u_1 = A \times cos(kx_1 - \omega t) \tag{14}$$

where the wavenumber is defined $k = \omega/c_L$, with c_L being the longitudinal wave velocity of the material. With this excitation, the partial differential equation in Equation 12 can be solved through perturbation analysis as [12]:

$$u_1 = \frac{1}{8}\beta k^2 {A_1}^2 x_1 + A_1 cos(kx_1 - \omega t) + \frac{1}{8}\beta k^2 {A_1}^2 x_1 cos(2kx_1 - 2\omega t)$$
$$= A_0 + A_1 cos(kx_1 - \omega t) - A_2 cos(2kx_1 - 2\omega t) \quad (15)$$

The third term in Equation 15 is information on the second harmonic wave and can be used to show the following relationship for the acoustic nonlinearity parameter:

$$\beta = \frac{8A_2}{k^2 x_1 {A_1}^2} \quad (16)$$

This expression shows that β can be measured from amplitudes of the fundamental (A_1) and second harmonic (A_2) signals, with information on the propagation distance (x_1) and the wave number. β is an absolute material constant that can give information to the state of material damage as shown in Equation 13.

2.4.2 Derivation of Nonlinearity Parameter for Rayleigh Waves

Equation 16 is an expression for the nonlinear acoustic parameter for a one-dimensional longitudinal wave. Rayleigh waves propagating in a solid contain both longitudinal and shear wave, with the shear motion being significantly more dominant. The displacements of these components can be decomposed as in Equations 17 and 18 as done by Herrmann et al. [18]. The x-axis is defined in the direction of wave propagation (longitudinal):

$$u_x(\omega_o) = A_1 \left(e^{-pz} - \frac{2ps}{{k_R}^2 + s^2} e^{-pz} \right) e^{i(k_R x - \omega t)} \quad (17)$$

and the z-axis is defined perpendicular to the material (shear):

$$u_z(\omega_o) = iA_1 \frac{p}{k_R}\left(e^{-pz} - \frac{2{k_R}^2}{{k_R}^2 + s^2} e^{-sz}\right) e^{i(k_R x - \omega t)} \tag{18}$$

where $p^2 = k_R^2 - k_L^2$ and $s^2 = k_R^2 - k_S^2$; and k_R, k_L , and k_S are the wavenumbers for Rayleigh, longitudinal, and shear waves respectively. Similarly, the Rayleigh waves produced by second harmonic generation can be described at sufficiently large propagation distances from the wedge as

$$u_x(2\omega_o) \approx A_2\left(e^{-2pz} - \frac{2ps}{{k_R}^2 + s^2} e^{-2sz}\right) e^{2i(k_R x - \omega t)} \tag{19}$$

and

$$u_z(2\omega_o) \approx iA_2\left(e^{-2pz} - \frac{2{k_R}^2}{{k_R}^2 + s^2} e^{-2sz}\right) e^{2i(k_R x - \omega t)} \tag{20}$$

A_1 and A_2 are the amplitudes of the fundamental and second harmonic waves in the respective equation. In isotropic materials, acoustic nonlinearity arises solely due to the longitudinal wave components (x-axis) because of symmetry conditions and the third order elastic constant vanishes for shear waves [8]. AM materials can display anisotropic behaviors caused by the layer-by-layer building approach [19]. Determining if the symmetry condition holds in the application of nonlinear ultrasonics to AM is a basis for the intellectual curiosity behind this work. Herrmann et al. derived the acoustic nonlinearity parameter, β, from the vertical displacements at the surface (z = 0) for the fundamental and second harmonic waves [8]:

$$\beta = \frac{\bar{u}_z(2\omega_0)}{\bar{u}_z{}^2(\omega_0)x}\frac{8ip}{k_L^2 k_R}\left(1 - \frac{2k_R{}^2}{k_R{}^2 + s^2}\right) \tag{21}$$

where $\bar{u}_z = u_z(z = 0)$. This equation comes from the previously derived nonlinearity parameter in Equation 16 and the longitudinal displacement fields given in Equations 18 and 20. The total acoustic nonlinearity parameter for Rayleigh waves is given in Equation 21 but in this equation the following proportionality can be seen:

$$\beta \propto \frac{\bar{u}_z(2\omega_0)}{\bar{u}_z{}^2(\omega_0)x} \tag{22}$$

This relative nonlinear parameter is the metric used in this study. The effects from attenuation and diffraction are assumed to be held constant for all samples as measurement techniques are consistent. Therefore, the relative β given in Equation 22 will be used to compare samples at different heat treatment states as the relative change in nonlinearity will correlate to the microstructural changes to be tracked.

2.5 Model of Microstructural Contributions to Ultrasonic Nonlinearity

Hikata et al. expanded models of the contributions of dislocations to β [11]. An edge dislocation segment is pinned between two points; pinning can occur from gran boundaries, point defects, and other dislocations. The distance between the two points is defined as 2L as seen in Figure 2. When a small longitudinal stress, σ, is applied, the dislocation segment bows into a circular arc defined by radius r and the angle θ, as seen in Figure 2.

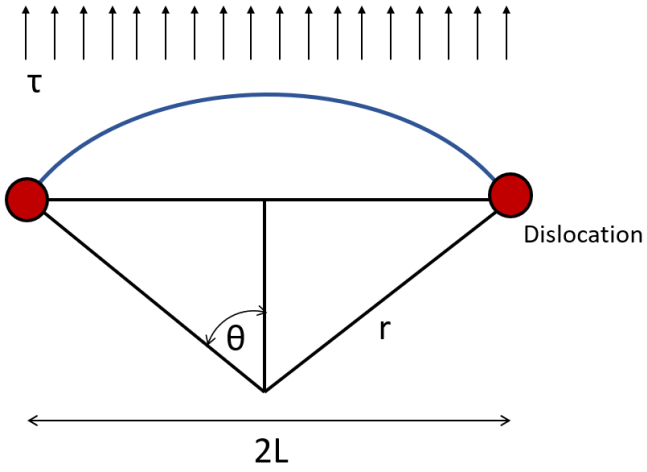

Figure 2: Stick figure representation of pinned dislocation segment with an applied shear stress, τ

The longitudinal stresses are small such that the dislocation segment stays pinned, such as the case with residual stress. The shear component of σ is defined by:

$$\tau = m\sigma \tag{23}$$

where m is the Schmid factor that describes the direction of slip and is defined by:

$$m = cos(\phi)cos(\lambda) \tag{24}$$

where ϕ is the angle of a vector normal to the glide plane and λ is the glide direction. The line tension, T, can be found from this shear by:

$$T = \tau r b = \frac{1}{2} G b^2 \tag{25}$$

where b is the Burger's vector and G is the shear modulus. The strain corresponding to the shear stress is found from:

$$\gamma = \frac{\Lambda b S}{2L} \tag{26}$$

where Λ is the dislocation density and S is the area swept by the dislocation segment that is approximated by:

$$S = r^2\left(\theta - \frac{1}{2}\sin(2\theta)\right) \tag{27}$$

The angle θ is assumed to be small and is defined from the geometry in Figure 2 as $\theta = \sin^{-1}(L/r)$. Using the definition of S in Equation 27 and the small angle assumption, the strain in Equation 26 can be found as:

$$\gamma = \frac{2\Lambda L^2 r}{3G} + \frac{4\Lambda L^4 r^3}{5G^3 b^2} \tag{28}$$

This strain is a component of the total strain in the material that is found by:

$$\epsilon_T = \epsilon_{lattice} + \Omega\gamma \tag{29}$$

where Ω is a conversion of the shear strain to its longitudinal equivalent. The total strain in the material can be written in the same form as the constitutive equation of internal stress for a material with quadratic nonlinearity of the form:

$$\sigma_{xx} = E_1\frac{\partial u}{\partial x} + \frac{1}{2}E_2\left(\frac{\partial u}{\partial x}\right)^2 \tag{30}$$

where E_1 and E_2 are the second and third order elastic constants, respectively. The resulting stress-strain relationship of the total stress is then written as:

$$\epsilon = \left(\frac{1}{E_1} + \frac{2\Omega\Lambda L^2 R}{3G}\right)\sigma + \frac{E_2\sigma^2}{{E_1}^3} + \frac{4\Omega\Lambda L^4 R^3 \sigma^3}{G^3 b^2} \tag{31}$$

The addition of a small ultrasonic stress, $\Delta\sigma$, will further deform the dislocation segment generating an additional strain, $\Delta\epsilon$. The addition of the small ultrasonic stress to the initial static stress (depicted in Figure 2) will cause a vibration of the dislocation segment. This additional stress and strain are related by:

$$\Delta\sigma = \frac{\partial\sigma}{\partial\epsilon}\Delta\epsilon + \frac{1}{2}\frac{\partial^2\sigma}{\partial\epsilon^2}(\Delta\epsilon)^2 \tag{32}$$

The strain-stress relationship in Equation 31 is inverted to get $\frac{\partial\sigma}{\partial\epsilon}$ and $\frac{\partial^2\sigma}{\partial\epsilon^2}$. When these are substituted into Equation 32, the additional stress is expanded to:

$$\Delta\sigma = \left[\frac{1}{E_1} + \frac{2\Omega\Lambda L^2 R}{3G}\right]^{-1}\Delta\epsilon - \left[\frac{E_2}{{E_1}^3} - \frac{12\Omega\Lambda L^2 \mathrm{R}\sigma}{5G^3 b^2}\right]\left[\frac{1}{E_1} + \frac{2\Omega\Lambda L^2 R}{3G}\right](\Delta\epsilon)^2 \tag{33}$$

From Equation 13, the acoustic nonlinearity parameter is the negative ratio of the first two coefficients. In the case of the small oscillatory applied stress, the total nonlinearity parameter is then:

$$\beta_{total} = \left[-\frac{E_2}{{E_1}^3} + \frac{24\Omega\Lambda L^4 \mathrm{R}^3\sigma}{5G^3 b^2}\right]\left[\frac{1}{E_1} + \frac{2\Omega\Lambda L^2 R}{3G}\right]^{-2} \tag{34}$$

In most materials, the assumption that $\frac{2\Omega\Lambda L^2 R}{3G} \ll \frac{1}{E_1}$ is true so that the total nonlinearity parameter can simplify to:

$$\beta_{total} = -\frac{E_2}{E_1} + \frac{24\Omega\Lambda L^4 \mathrm{R}^3 {E_1}^2 \sigma}{5G^3 b^2} \tag{35}$$

The ratio of $-{E_2}/{E_1}$ is the lattice contribution of nonlinearity so the change in β due to changes in dislocation pinning is:

$$\beta_{total} = \frac{24\Omega\Lambda L^4 \mathrm{R}^3 {E_1}^2 \sigma}{5G^3 b^2} \tag{36}$$

This relation shows that β is theoretically sensitive to changes in dislocation density, Λ, which this work hopes to verify for AM materials.

2.6 Derivation of Acoustic Attenuation

Acoustic attenuation is an intrinsic material parameter that can dramatically affect the propagation of acoustic waves through a solid. Material composition, crystal grain structure, and inhomogeneities such as precipitates are some of the material properties which influence attenuation. Acoustic attenuation and its correlation to microstructure are often used in NDE. Extensive research has been done in the NDE field to connect attenuation to mechanical properties for monitoring of critical systems; one of the most common family of materials in these applications are austenitic stainless steels.

Some of the initial work of attenuation in austenitic stainless steel where lead by R.L. Smith at the National NDT Centre in the United Kingdom [20]. In the first of his papers

reviewed in this work, Smith studies the effects of grain size on ultrasonic attenuation and its frequency dependence [20]. A few years later, the same research group began looking at the possibilities of material characterization based on ultrasonic attenuation [21]. Relative acoustic attenuation is used in this thesis as a complimentary linear measurement to NLU.

Acoustic attenuation is a property encompassing two different effects in a material. As a wave passes through a material, energy can be lost through absorption and scattering [20]:

$$\alpha(f) = \alpha_a(f) + \alpha_s(f) \tag{37}$$

where $\alpha_a(f)$ is the absorption contribution to attenuation caused by features including dislocation damping and thermoelastic interactions, and $\alpha_s(f)$ is the scattering contribution from interactions with features including voids and grain boundaries. f is the frequency for which attenuation is dependent upon [20]. For most media including stainless steels, wave amplitude decreases with propagation due to attenuation. This effect is accounted for in the 1D wave particle displacement equation with the form:

$$u = Ae^{(-\alpha Z)}e^{i(\omega t - kZ)} \tag{38}$$

To determine the attenuation coefficient of a material, first the wave speed in the material needs to be measured. The wave speed is measured for each specimen and by measuring the time difference between the initial wave packet and the first reflection:

$$c = \frac{2z}{t_1 - t_2} \tag{39}$$

where z is the sample thickness and t_1 and t_2 are the temporal locations of the same point on two contiguous packets. The magnitude for complex frequency spectra of each packet can be found from [22]:

$$s_n(f) = \frac{\lambda \times \Delta x}{(r_{trans})^2} \tag{40}$$

where λ is the wavelength of the signal found using the wave speed from Equation 393939 and the inputted frequency. Δx is total distance travelled by the corresponding wave packet, and r_{trans} is the radius of the transducer. Equation 40 is used to calculated magnitudes of the complex diffraction correction functions corresponding to the propagation distances of these signals, D, as described by Rogers and Van Buren [23]:

$$D(s_n) = 1 - 2^{-i(2\pi/s_n)}\left[J_o\left(\frac{2\pi}{s_n}\right) + iJ_1\left(\frac{2\pi}{s_n}\right)\right] \tag{41}$$

where J_n is a Bessel function of the first kind of order n. Equation 41 and the voltage ratio between wave packets can be used to calculate the attenuation coefficient:

$$\alpha(f) = \frac{1}{2z}\left[\ln\left(\left|\frac{v_1}{v_2}\right|\right) - \ln\left(\left|\frac{D(s_1)}{D(s_2)}\right|\right)\right] \tag{42}$$

Where v_1/v_2 is the measured voltage ratio between the steady state portions of the first and second wave packets. This attenuation measurement does not correct for losses between

the transducer and material surface; however, with a consistent experimental setup, the largest contribution to the variation between each specimen's attenuation will come from the material itself. Thus, these values are used as a relative attenuation measurement to compare between the specimens in this work.

CHAPTER 3. SPECIMENS

3.1 Testing Specimens

Four specimens varying in material composition and manufacturing technique are used in this study: two are made of 316L grade stainless steel, and two of 304L grade stainless steel. For each stainless steel variant, one specimen is made with an AM technique and the other is a traditional wrought manufactured for comparison purposes; see Table 1 for details.

Table 1: The four specimens and the corresponding manufacturing technique and metal variant

	316L	**304L**
Additive Manufactured	316L PBF	304L LENS
Wrought	316L Wrought	304L Wrought

AM Specimens were manufactured at Sandia National Laboratories for this work. The wrought manufactured specimens were obtained from multiple commercial suppliers and may have different metallurgical histories.

The test specimens are flat bars with varying dimensions. All the specimens are approximately 0.5” thick by 2” wide and a length of 6”. The thinnest sample is the 316L PBF specimen with a thickness of 1 cm as measured after all surface preparations. Rayleigh wave displacement decays rapidly with depth and is negligible beyond a depth of 1.5λ [15,24]. The input wavelength is approximately 2.64 mm; therefore, the Rayleigh wave

displacement would be negligible deeper than 0.396 cm and the wave will propagate without any reflections from the bottom surface.

3.1.1 Stainless Steel Variation

316L and 304L variants of stainless steel are among the most popular variants of stainless steel used. Both are classified as austenitic variants with a face-centered cubic structure. All four specimens are L variants which indicates a carbon content no more than 0.04% carbon. The low carbon content aids in preventing carbide precipitation which can lead to corrosion [25]. The difference in stainless steel comes from the different chemical composition as seen in Table 2.

Table 2: Typical chemical composition of stainless alloys in wt.% [26]

Chemical	**C**	**Co**	**Cr**	**Cu**	**Mn**	**Mo**	**N**	**Ni**	**P**
304L	.04	0.17	18.10	0.29	1.25	0.22	.08	8.15	0.03
316L	.02	0.19	16.92	0.28	1.30	2.01	.04	10.38	0.03

The 304 alloys of stainless steel are the most widely used of the austenitic type; uses can vary from light chemical storage to consumer products [27]. The addition Nickel (Ni) and Molybdenum (Mo) in 316 alloys provide better corrosion resistance than 304 alloys [27]. Both alloys are extensively used in the nuclear energy field [28], where a large need for NDE exists.

3.1.2 Additive Manufacturing Methods

Two different additive manufacturing techniques are investigated in this study.

3.1.2.1 Powder Bed Fusion

A ProX DMP 200® printing system was used to make the 316L AM specimen through laser powder bed fusion (L-PBF). In L-PBF, a thin layer of metal powder is spread across the print surface and then transformed into the desired solid material shape with a laser energy source through rapid melting and solidification. The specimens in this study are produced using a 3D Systems "hexagon" scan pattern where the laser scans within interconnected 10 mm diameter circumscribed hexagons, see Figure 3. These hexagons are stitched together to create one layer of the print. The next layer is then deposited, and the process is repeated layer by layer until the part is manufactured. The piece was cut from the build plate with a wire EDM machine.

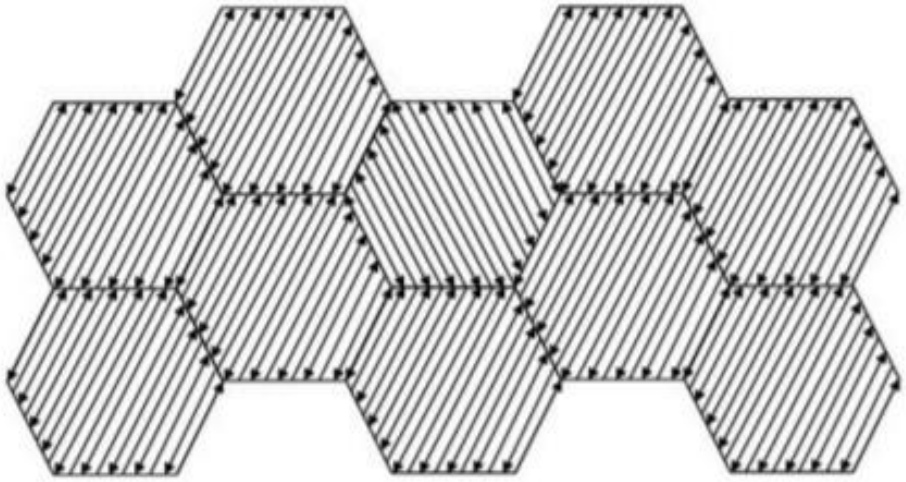

Figure 3: L-PBF hexagon printing pattern. Arrows point in back and forth scanning of laser to create each individual hexagon. [29]

The printing parameters used in the creation of this specimen are found in Table 3.

Table 3: L-PBF Printing Parameters

Laser Power	103W
Velocity	1400 mm/s
Laser Beam Nominal Diameter	100 μm
Layer Thickness	30 μm
Hatch/Cross Feed	50 μm
O_2 Setpoint	1000ppm
Build Chamber Temperature	38ºC

The powder used in this print was on its 15th use cycle. Reuse of powder is commonly used to reduce the cost associated with AM but can have slight microstructural effects in L-PBF [30]. The powder size distribution is seen in Table 4. D50 is defined as the median distribution of partial size. D10 is defined at the tenth percentile of powder size and similarly, D90 is at the 90th percentile [31].

Table 4: Powder size distribution

Distribution Width	**Size (μm)**
D10	11.8
D50	18.1
D90	27.9

3.1.2.2 Laser Engineered Net Shaping

The 304L AM specimen is manufactured by laser Directed Energy Deposition (DED) in a Laser Engineered Net Shaping (LENS) 750 (Optomec Inc., USA) workstation. Multiple nozzles are used to blow metal powder into the path of a co-axial vertical laser. The thermal source and nozzles are co-located which allows for complex shapes to be built

in a short time [1]. This sample was provided for this study and the manufacturing details are not known. The build plate was left on the sample for the NLU measurements; for each sample cut for EBSD, the build plate was removed with wire EDM.

3.1.3 AM Microstructural Challenges

Besides the creation of creation of residual stress and dislocations discussed in Section 1.1, the thermal history associated with AM can lead to anisotropy and heterogenous microstructure [5]. Different areas of an AM build will have different cooling rates dependent on that areas ability to conduct, convect, or radiate heat [4]. Post-processing can remove some of this anisotropy. β is theoretically derived for this thesis for an isotropic material but has been successfully used on commercially available metals with natural inhomogeneity. Furthermore, similar non-contact Rayleigh wave SHG setups have been used on highly inhomogeneous materials including concrete [32].

Austenitic stainless steels made with traditional manufacturing methods are primarily composed of equiaxed austenite grains with some ferrite stringers [5]. In comparison, the rapid cooling associated with AM causes elongated grains in the direction of build and are similar to the microstructure resultant from welding [5]. Incomplete powder fusion can create voids in the microstructure with the potential to scatter ultrasonic waves.

3.2 Heat Treatment Plan

An annealing heat treatment is used to cause microstructural changes and reduce dislocation density in the specimens. A comparative study of 304L LENS and 304L

wrought by Smith et al. [33] observed a significant decrease in dislocation density. These microstructural changes were first observed in hardness measurements, as seen in Figure 4, that were later confirmed with EBSD imaging. The 304L LENS sample is labeled as DED 304L referencing the Directed Energy Deposition category of AM which includes the LENS systems. Following this work, Susan et al. used a similar heat treatment profile for 316L PBF samples [34].The process conditions are expectedly similar between analogous alloys used in these studies and this work.

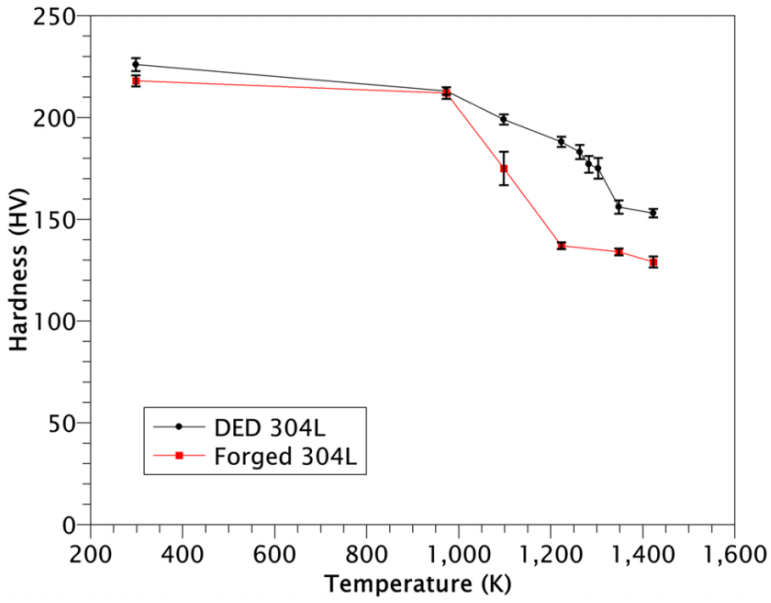

Figure 4: Hardness as a function of annealing temperature from Smith et al. [33]

Using the results of [33], a similar heat treatment plan is developed and listed in Table 3, with an x-mark indicating where accompanying β measurements are made. The 316L PBF and 316L Wrought specimens have finer temperature increments to allow for a more detailed comparison between the two manufacturing methods.

The first three heat treatments are performed in near-vacuum stainless steel bags to prevent oxidization on the specimen surface. The final heat treatment was performed in a vacuum

furnace that allowed for the high temperature with an Argon atmosphere. Following the heat treatment, each specimen is gradually brought to room temperature.

Table 5: Heat Treatment State of Measurement

Specimen	As Received	650°C, 0.5 hr	950°C, 0.5 hr	1050°C, 0.5 hr	1200°C, 2.5 hrs
316L PBF	x	x	x	x	x
316L Wrought	x	x	x	x	x
304L LENS	x			x	x
304L Wrought	x			x	x

3.3 Surface Treatment

All specimens are initially surface ground to have parallel top and bottom surfaces. By doing so, the liftoff distance of the air coupled transducer remains contain throughout the measurement as explained in Chapter 4. Following each heat treatment, the specimens are hand polished to a finish of 1500 grit. This surface finishing removes any oxidization that may have occurred and significantly increases the signal-to-noise ratio (SNR).

CHAPTER 4. EXPERIMENTAL PROCEDURE

4.1 Rayleigh Wave Measurement

4.1.1 Experimental Setup

A schematic of the nonlinear air-coupled detection Rayleigh wave experimental setup is shown in Figure 5. A function generator outputs a sinusoidal tone burst signal at 2.1 MHz with a peak to peak voltage of 800 mV. This signal consists of 20 cycles with a spacing of 20 ms which provides a long stable signal between transient states of material ringing up and down. This stable signal is later needed for signal processing.

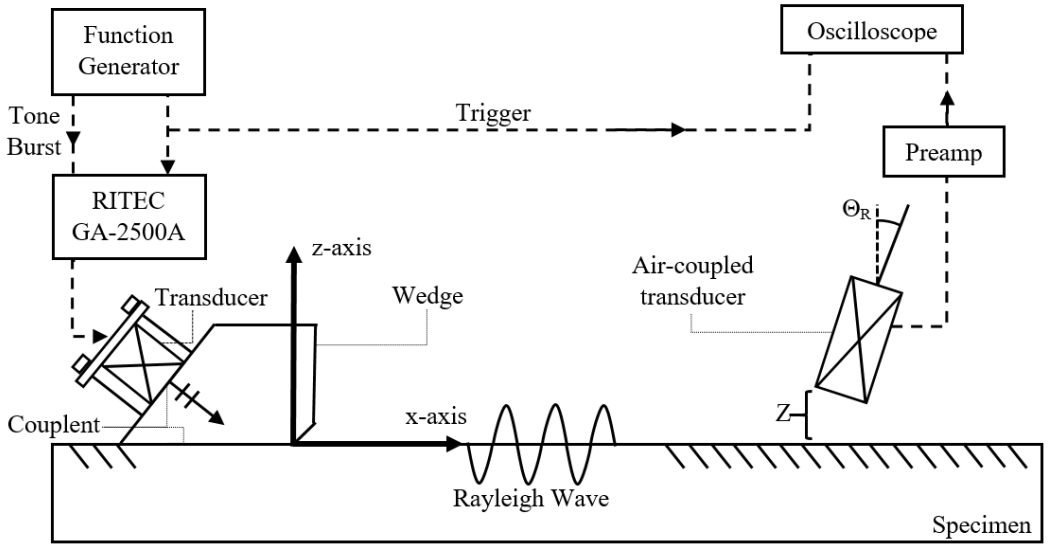

Figure 5: Nonlinear ultrasound with Rayleigh wave measurement setup. Dashed lines indicate wiring setup of electrical equipment.

The output from the function generator is amplified through a high-power gated amplifier (RITEC GA-2500A). This system increases the acoustic energy of the input signal which in turn increases the SNR of the output measurement. The system is turned

on 30 minutes prior to measurements to reduce system nonlinearity and to increase the stability of the outputted signal. The high voltage excitation from the amplified system is connected to the outputting transducer

A Parametrics V106 (2.25 MHz nominally centered) contact transducer generates a longitudinal wave from this signal into an acrylic wedge that is coupled to the surface of the test specimen. The acrylic wedge is cut to a specific geometry (defined in Figure 6) to maximize the transmission from the traditional P-wave transducer into a Rayleigh surface wave. Based on Snell's law, a Rayleigh surface wave can be generated from an inputted longitudinal wave through a wedge. The wedge in these measurements was made from a plexiglass material cut to a specific geometry for stainless steels as seen in Figure 6. As the Rayleigh wave travels parallel to the material-wedge interface, the angle of the wedge can be found from:

$$\theta_{p1} = \arcsin\left(\frac{C_{p1}}{C_{R2}}\right) \tag{43}$$

where θ_{p1} is the incoming longitudinal angle defined in Figure 6, C_{p1} is the longitudinal wave speed in the acrylic wedge, and C_{R2} is the Rayleigh wave speed in the specimen.

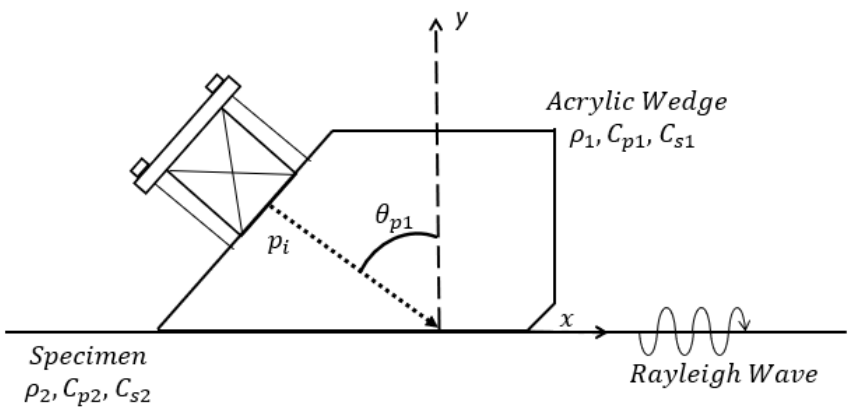

Figure 6: Definition of Wedge Geometry

All contact surfaces between the transducer, wedge, and specimen are coupled with an oil based couplant. Constant contact between these surfaces is achieved with a clamping mechanism. The physical setup is allowed to settle for 30 minutes prior to measurement to allow for any spreading of the couplant caused by the clamping force. After this time, the thickness of the couplant layer remains largely constant throughout the measurement period.

The Rayleigh surface wave travels along the surface of the specimen and interact with the material microstructure, creating a second harmonic. Leaked Rayleigh waves are then detected with an Ultran NCT4-D13 (4 MHZ nominally centered) air-coupled transducer. The frequency response of this receiving transducer dictates the frequency of the input wave to be 2.1 MHz as the second harmonic at 4.2 MHz is at the maximum response of the air-coupled transducer.

The air-coupled transducer is connected to a 6 degree of freedom stage. From this stage, the transducer angle (θ_R in Figure 5) associated with the maximum fundamental

frequency response is found and held constant during the measurement. A liftoff distance (Z in Figure 5) of 3mm is also held constant.

Material nonlinearity will cause an increase in β with increasing propagation distance, while any initial system nonlinearity remains constant as a function of propagation distance [35]. This allows the material contribution to the acoustic nonlinearity to be isolated from the system nonlinearity, if a measurement path of increasing propagation distance is found. A calibration procedure is performed to find a measurement path that maximizes the fundamental frequency signal, see Figure 7. The Rayleigh wave beam is not centered on the exact midpoint of the emitting wedge, nor is perfect alignment between the wedge and sample feasible. This path is found by finding the x_{start} corresponding to a maximum fundamental response at the beginning of the far field. The far field for this system is determined to be 3 mm from the leading edge of the wedge. The x_{end} is found at the maximum fundamental response at a y position further down the specimen. This distance is typically set to 50mm if specimen geometry allows, as 50mm of propagation includes enough measurement points to accurately measure β. For some specimens, a propagation distance of 50mm would lead to reflection effects from the trailing edge of the specimen. In these cases, the maximum propagation distance before potential edge effects was used and the measurement frequency along the propagation path was increased.

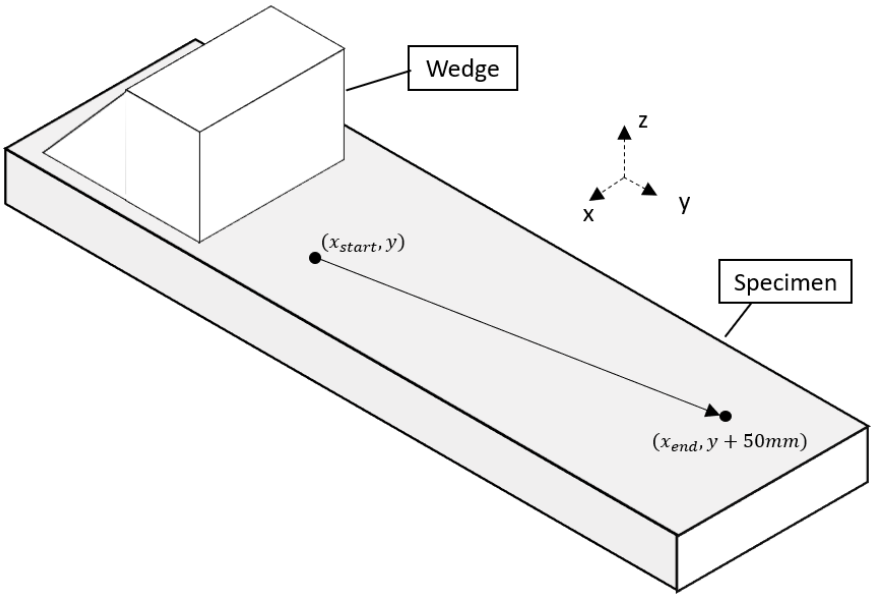

Figure 7: Calibration Geometry for Rayleigh wave testing

4.1.2 Measurement Processing

The output from the air-coupled transducer can be seen in Figure 8 in the time domain. This recorded signal is post amplified and averaged 512 times to increase SNR. A Hann window is applied to reduce the transient effects of voltage overshoot and ringing that can be seen in the air-coupled transducer output [36]. This Hann window isolates the analyzed portion of the signal to the steady cycles seen in the time domain.

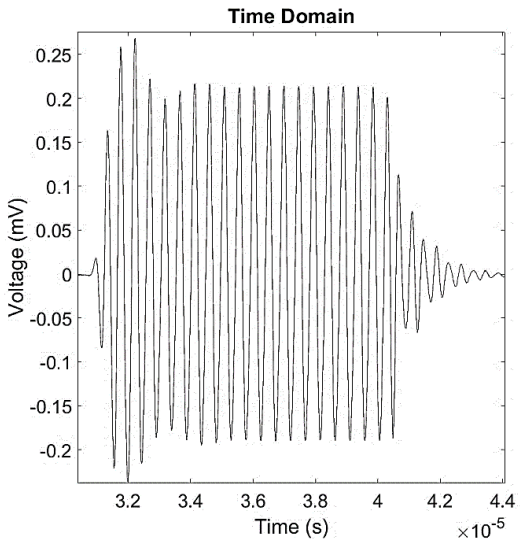

Figure 8: Time averaged base signal measured from air coupled transducer

A Fast Fourier transform (FFT) transforms the time-domain signal into the frequency spectrum as seem in

Figure **9**. The two distinct peaks are centered at the fundamental frequency of 2.1 MHz and the second harmonic of 4.2 MHz. As expected, the amplitude of the fundamental frequency is much higher than that of the second harmonic.

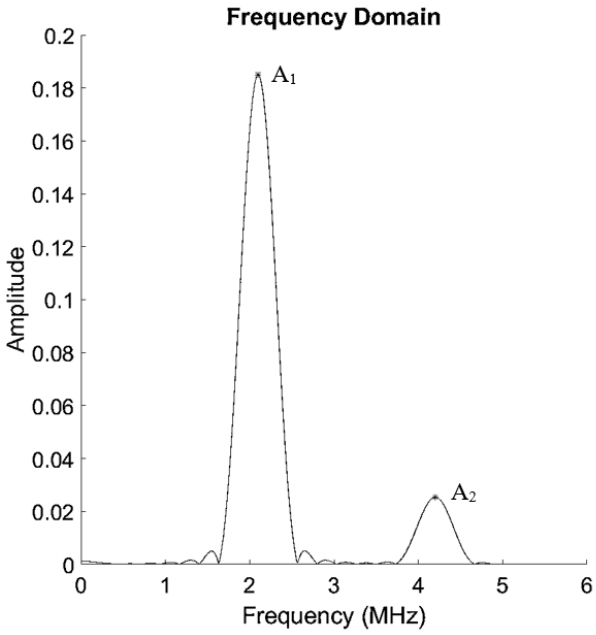

Figure 9: FFT results after Windowing

Figure 10 shows that the amplitude of the fundamental frequency decreases with increasing propagation distance from diffraction effects. Conversely, the second harmonic increases with propagation distance, as the wave continues to interact with the material microstructure. The ratio of these two frequencies are used are used in Equation 22 to calculate the relative acoustic nonlinearity parameter, β. A graphical representation of the ratio of these two peaks as a function of propagation distance is seen in Figure 11. The slope of this line is taken as the relative nonlinearity parameter, β.

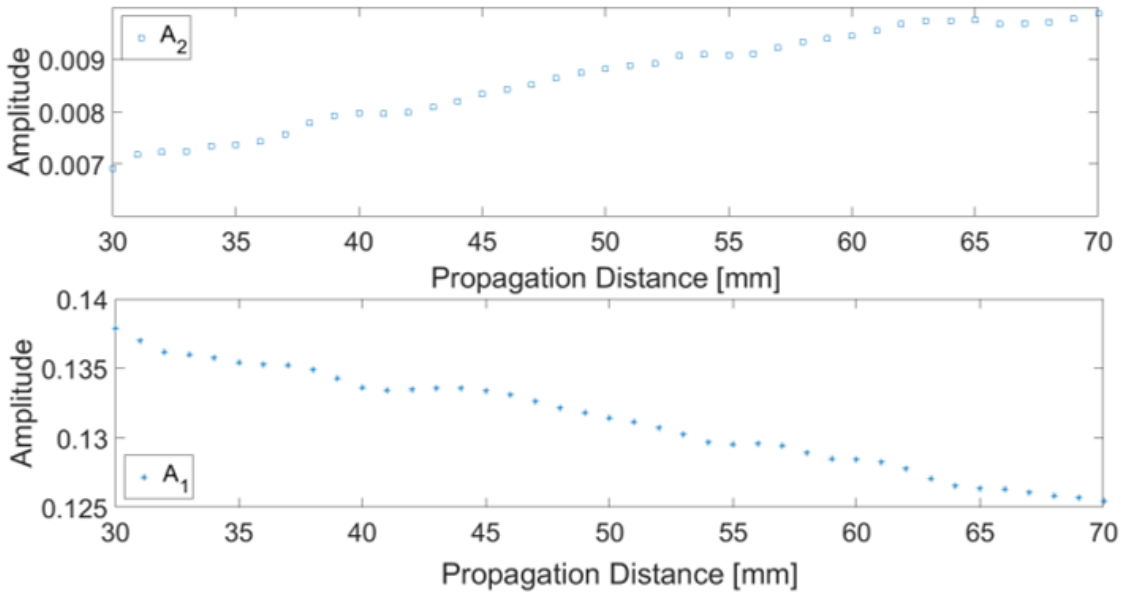

Figure 10: The second harmonic, A2, and fundamental frequency, A1, as functions of the propagation distance

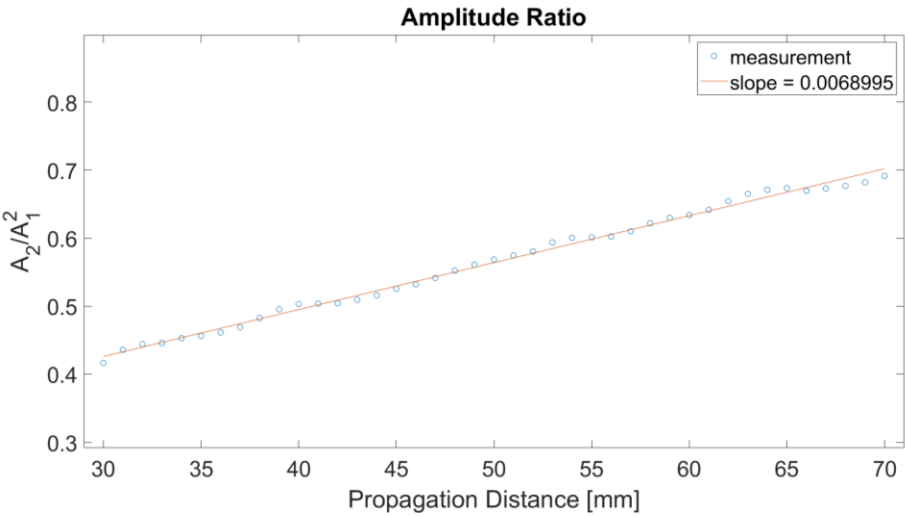

Figure 11: Example result of a Rayleigh wave measurement. The nonlinearity parameter for one measurement is found from slope of this plot.

4.2 Hardness Testing

Vickers microhardness measurements [37] were performed on the polished as-built and annealed specimens. These measurements were made by Sandia National Laboratories for this study. The Vickers measurements were performed with a 300g load and 15 second dwell time using a Struers DuraScan-80 microhardness mapper. The average and standard deviation of ~15 to 40 hardness measurements are reported from each specimen.

4.3 Electron Backscattering Diffraction

After each stage of heat treatment and NLU measurement, specimens were cut from the 316L PBF specimen material and mounted in cold-setting epoxy and prepared metallographically using standard techniques to enable microstructure observation and EBSD [38]. The EBSD specimens were sectioned normal to the AM build direction. A Zeiss Supra 55VP field emission scanning electron microscope (SEM) was used to perform EBSD using Oxford HKL Aztec^{TM} software. For all samples, EBSD data was collected using a stepsize of 0.1 μm. EBSD data were subsequently analyzed using MTEX [39], an extension for MATLAB^{TM}. EBSD data and subsequent GND measurements were collected by Philip Noell of Sandia National Laboratories for this study.

4.3.1 Geometrically Necessary Dislocation Measurement

Geometrically Necessary Dislocations (GNDs) are dislocations required to accommodate curves in the crystal lattice caused by plastic deformation [40]. As discussed by many others, *e.g.* see [41,42], these dislocations can be estimated from the curvature seen in EBSD data. GNDs have been shown to account for the majority of the total dislocation population in face-centered cubic metals [33]. Therefore, tracking the changes

in GND density can give indication to the relative changes in dislocation populations for comparison with β.

Because this measurement is sensitive to the step size used for data collection, direct comparison of GND density between different materials requires that all data be collected using the same step size, as was done in this study. Moreover, it is important to note that EBSD only provides an estimate for the lower bound of the GND density in a sample. The method presented by Pantleon [43] as implemented in MTEX [39] was used in this study to measure the lower bound of the GND density in as-built and annealed stainless steel specimens. It is important to note that, while this approach is slightly different from that used by Smith *et al.* [33], both approaches provide similar results [44]. A visual map of the distribution of GNDs using the EBSD data is presented in Section 5.5.

4.4 Acoustic Attenuation Measurements

The attenuation for each specimen is measured using contact transducers in a through transmission setup as seen in Figure 12. Two ultrasonic transducers, one transmitting and one receiving, are clamped through the thickness of the material with an oil based couplant between each contact surface. The surfaces are ground to ensure they are parallel and polished to provide a flat surface for good contact. Two wave packets are examined for each measurement; the first signal (labeled 1 in Figure 12) travels through the thickness of the specimen once, while the second (labeled 2 in Figure 12) travels through the sample three times. For each measurement, the attenuation coefficient is measured for a sweep of frequencies from 8 MHz to 20 MHz, changing the wavelength seen in Equation 40. The

trend of attenuation as a function of frequency is then compared between each sample and heat treatment state.

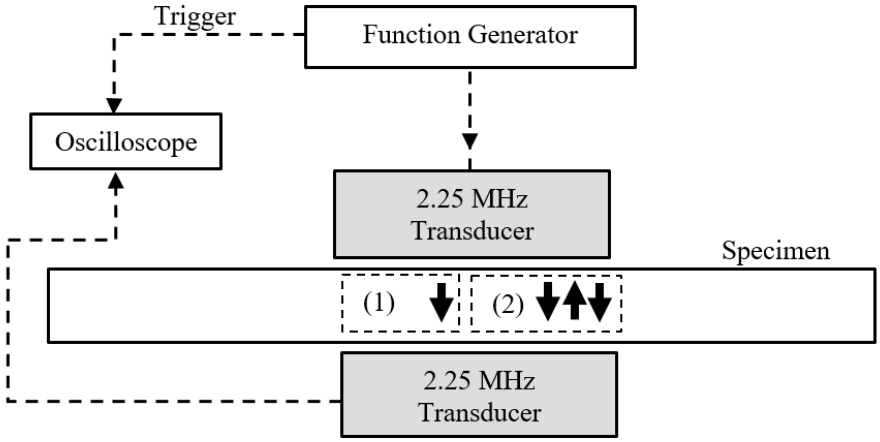

Figure 12: Through transmission attenuation measurement setup. Dashed boxes labeled 1 & 2 in specimen show path taken from first and second wave packet.

CHAPTER 5. RESULTS AND DISCUSSION

5.1 Overview

The results for each type of measurement are first presented in this chapter, then the relationship between these results are discussed. Results for the final recrystallization heat treatment are presented separately as they deviate from visible trends and may be associated with unique microstructural development.

5.2 Nonlinear Ultrasound Results

Following the heat treatment plan described in Table 5, β is measured for each specimen at each heat treatment stage, and the results are shown in Figure 13. Each box plot represents the results of five independent measurements at each stage in the heat treatment cycle. To make each measurement independent, the electrical equipment is restarted, the transducers are reattached, and the sample is remounted for each measurement.

The vertical axis is normalized to the lowest measured value of β. This normalization is performed as only the relative changes in β are considered with this experimental setup using the relation given in Equation 22. The results of β after the 1200°C heat treatment may be associated with entirely different microstructural changes caused by recrystallization and are analyzed separately in Section 5.7. Before complete recrystallization, β is shown to decrease with each consecutive heat treatment in each specimen, regardless of manufacturing technique. This trend is expected, as the annealing profile was selected to reduce dislocation density and other sources of material nonlinearity with increasing temperature and holding time.

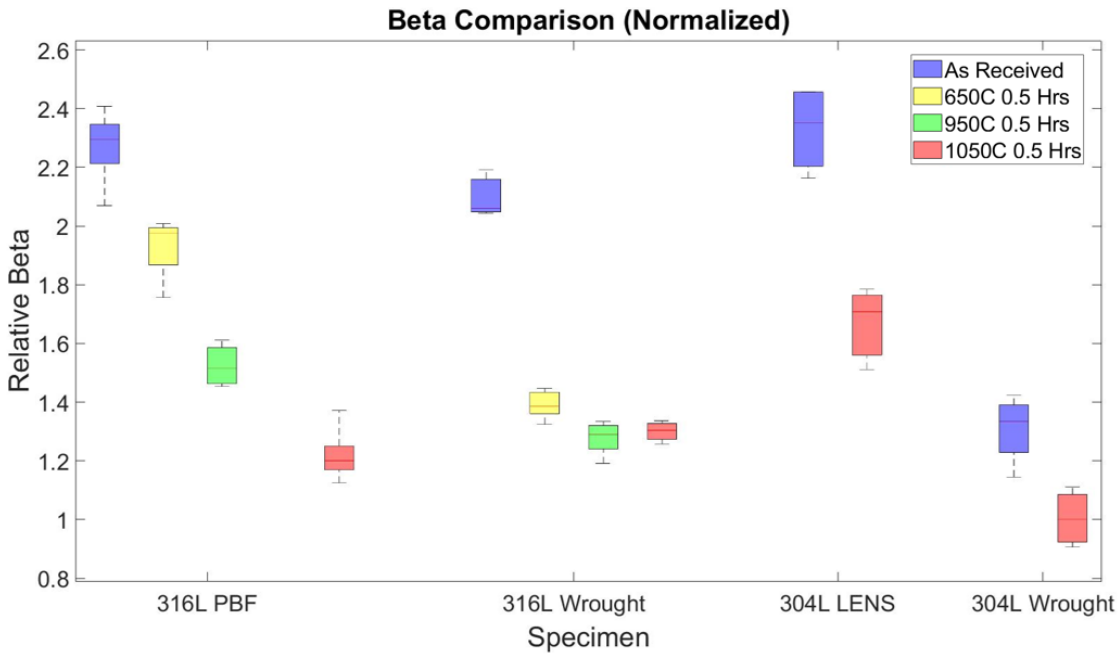

Figure 13: A box plot chart comparing normalized β values for each specimen through the heat treatment profile.

The finer increments in heat treatment profile for both the 316L PBF and 316L Wrought specimens allows for a comparison to be made between AM and traditional manufacturing techniques. Prior to complete recrystallization, the measured β linearly decreases in the 316L PBF specimen. Conversely, β in the 316L Wrought specimen begins to plateau after the heat treatment at 650°C (923 K) for 0.5 hours. As β is a surrogate for microstructural characteristics in a specimen, the different trends indicate a difference in microstructural evolution between the manufacturing techniques. These differences were previously observed by Smith et al [33] in their comparison of 304L AM and wrought. Figure 4, from Smith et al [33], shows the difference in hardness measurement trends between wrought and AM specimens through the heat treatment profile. The 304L Forged specimen drops in hardness faster than the DED 304L, and then begins to plateau while the DED specimen continues to decrease. The plateau seen in their hardness measurements is similar to the

plateau seen in the β measurements when comparing the 316L Wrought and 316L PBF specimens.

5.3 Hardness Results

The overall trends in hardness through the heat treatment are shown in Figure 14 for the 316L samples. Hardness of 316L PBF is consistently higher than its traditionally made counterpart; this trend is consistent in literature [5,33,34] and is attributed to the finer microstructural features resultant from powder-bed AM techniques [5]. Other potential causes of increased AM hardness include the higher dislocation density and residual stress [5], which could explain the decrease in hardness after annealing. Differences in hardness between these samples and those used by Susan et al. [34] may come from manufacturing and processing differences.

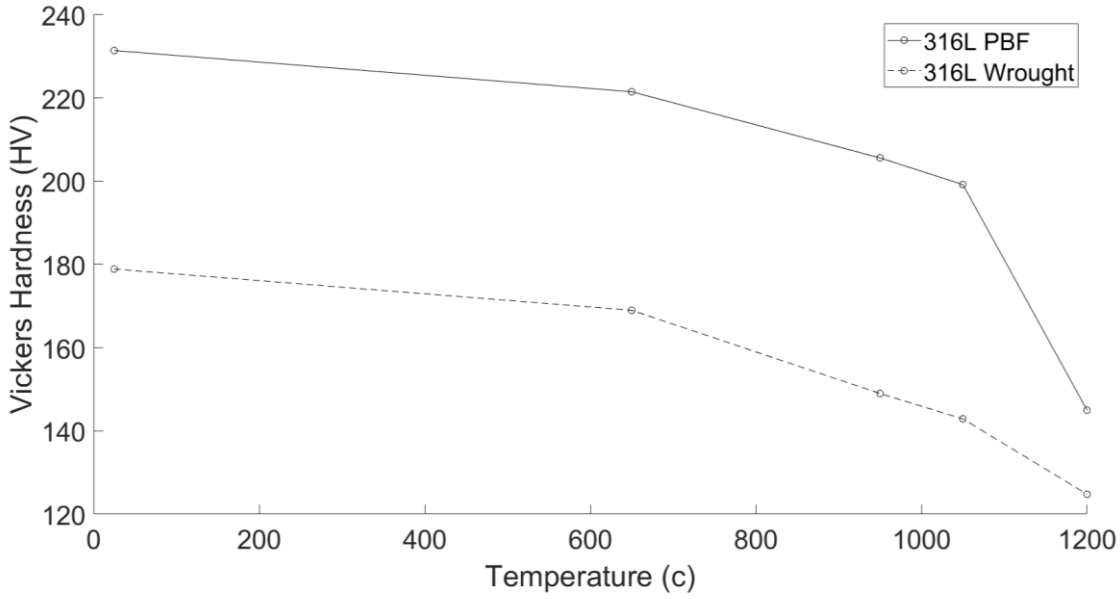

Figure 14: Vickers hardness comparison between 316L AM and Wrought through heat treatment

β appears to have an excellent correlation with hardness of the material. The two metrics are plotted concurrently in Figure 15, with a correlation coefficient of 0.997. Note that hardness is a macroscopic consequence of the dislocations as well as other features (grain boundaries) in the microstructure. Comparison of hardness and β over the different heat treatment stages shows a potential that both metrics are sensitive to similar microstructural features.

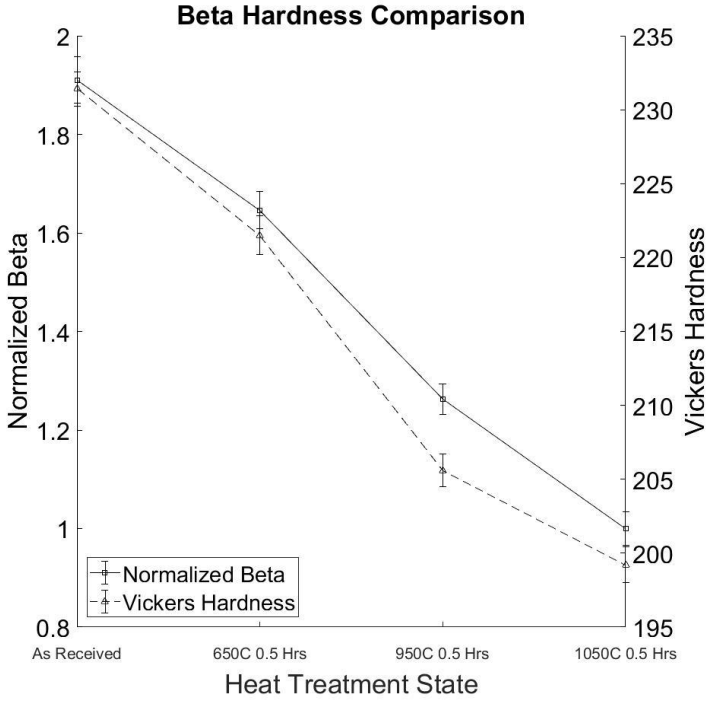

Figure 15: Hardness and β plotted concurrently of 316L PBF

5.4 EBSD Results

Microstructural evolution can be seen qualitatively in the inverse pole figure orientation mapping (IPF-z) results from EBSD for the 316L PBF sample in Figure 16. In these figures, the samples are oriented in a transverse direction with the build direction coming out of the page. This orientation results in showing a crosshatch scan pattern. These

images are each taken from different cuts of the main 316L PBF and are scanned at the same general location within each slice, so the changes in each individual grain and boundary cannot be tracked but the general trends between heat treatment steps can be observed. Only minor changes in the grain size can be seen up to the 1050°C heat treatment. EBSD was only performed for the 316L PBF sample due to budget constraints.

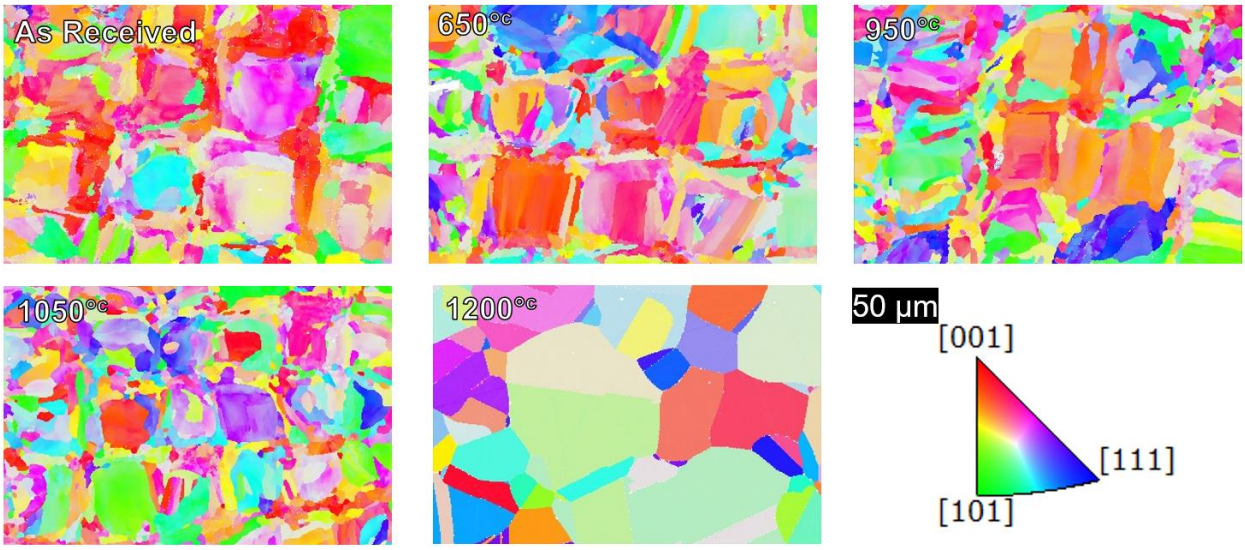

Figure 16: Inverse pole figure-z (IPF-z) orientation mapping of 316L PBF specimens

5.5 GND Measurement Results

A visual map of the distribution of GNDs in the 316L PBF sample can be seen in Figure 17 with grain boundaries colored black. GNDs are shown to decrease through the progression of heat treatments.

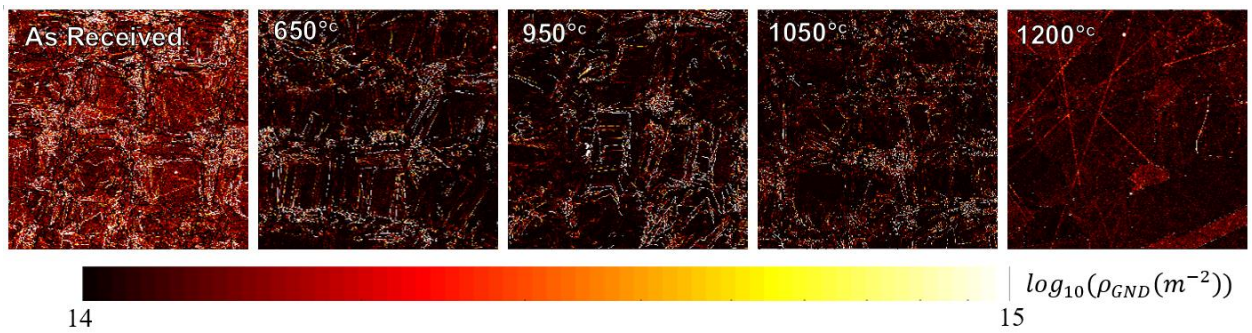

Figure 17: Geometrically necessary dislocation density mapping of 316L PBF specimen

By comparing the probability distribution functions of the GND density between material states, GND density can be quantitatively compared. The minimum GND densities averaged over the grains for the 316L PBF sample are plotted in Figure 18 for each material state in comparison with the measured β before recrystallization. The correlation coefficient between these two variables before the final recrystallization is 0.852. While β is sensitive to dislocations as predicted by the Hikata model [11] and others, it is also sensitive to other microstructural features [8]. Furthermore, GNDs do not account for all dislocations within the microstructure, also contributing to any deviations between β and the comparative measure.

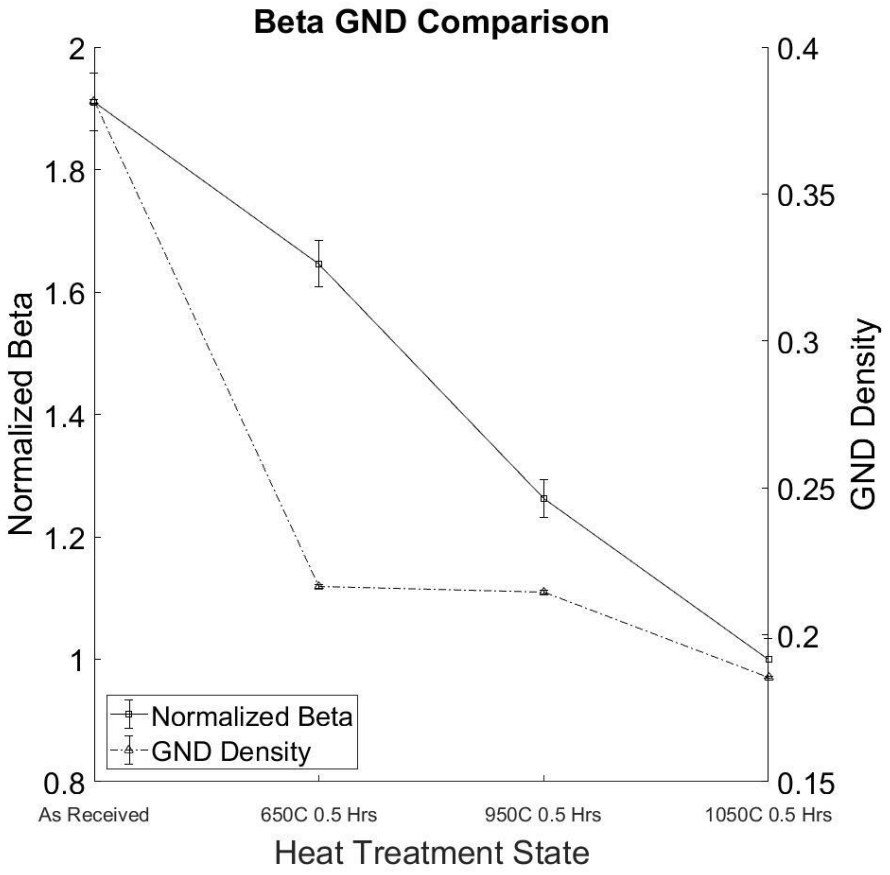

Figure 18: Mean GND density and β plotted concurrently of 316L PBF

5.6 Attenuation Results

Attenuation measurements for each sample at all material states were made; a comparison of each sample before heat treatment is seen in Figure 19. Before any heat treatments, both AM specimens had higher relative attenuation than the wrought counterparts. This may be caused by voids formed during printing and smaller grain size associated with the AM process [34]. The relationship between grain size and ultrasonic wavelength is known to contribute to the effects of scattering of the acoustic wave [45,46].

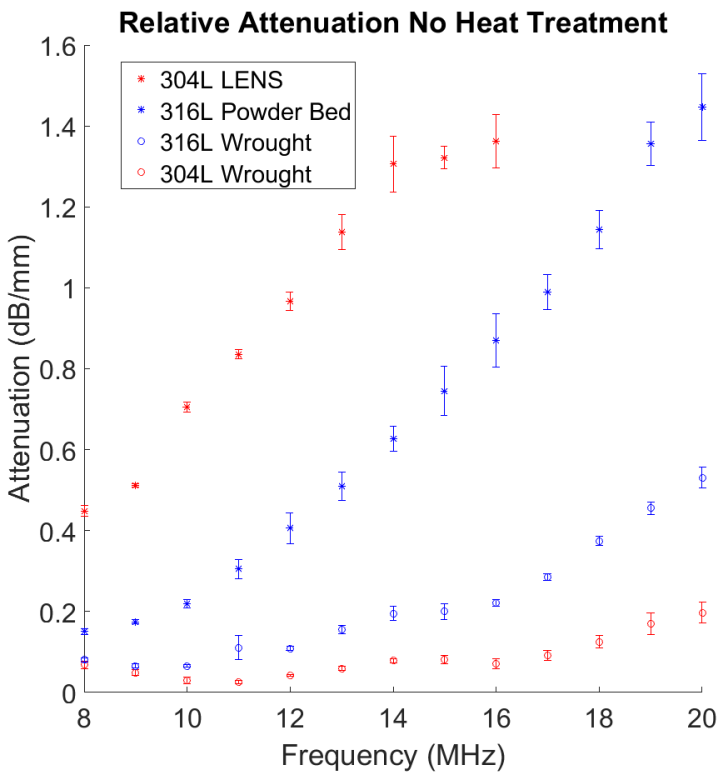

Figure 19: Acoustic attenuation of each sample prior to heat treatment

After heat treatment to 1050°c, the differences in attenuation between AM and wrought were once again apparent. In Figure 20, the separation between samples and heat treatment states at low frequencies is difficult. At higher frequencies, one noticeable trend is apparent; the attenuation of both AM specimens decreased after the 1050°c, whereas the attenuation of the wrought counterparts both increased.

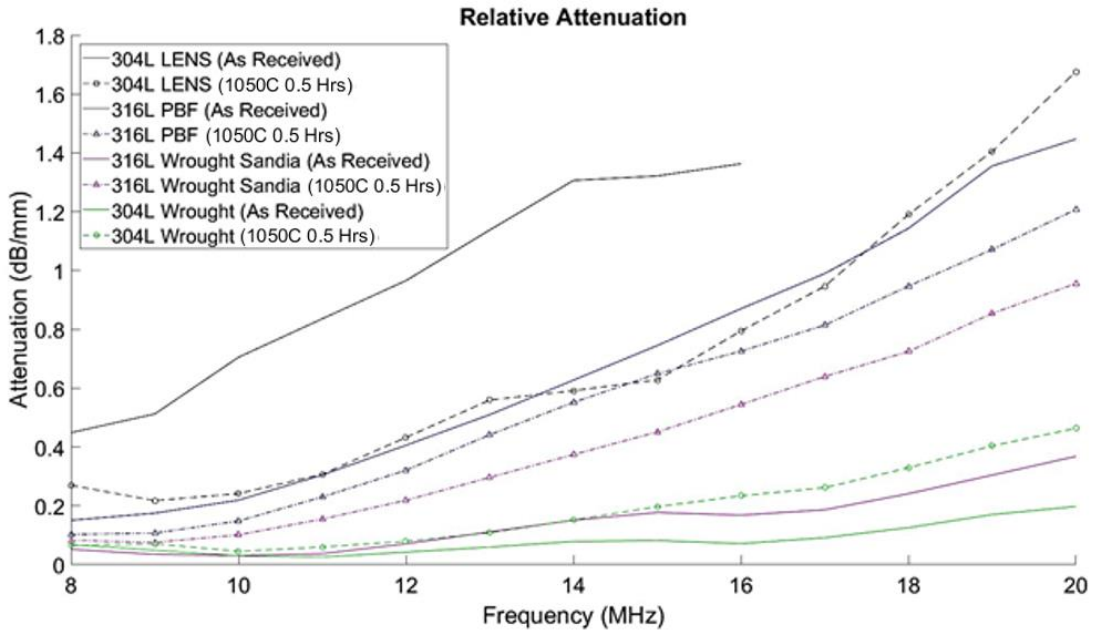

Figure 20: Acoustic attenuation as received and after penultimate heat treatment

When looking within a single specimen, these measurements of acoustic attenuation do not provide significant differentiation between heat treatment steps. Figure 21 shows the attenuation of 316L PBF at all heat treatment steps. The change of attenuation through the heat treatments does not appear to follow a pattern of increase or decrease. Below the 20 MHz range, these attenuation measurements are not highly sensitive to the material changes caused by annealing where the characteristic length (the grain size) is an order of magnitude smaller than the wavelength of the ultrasonic wave (~300 μm) [46].

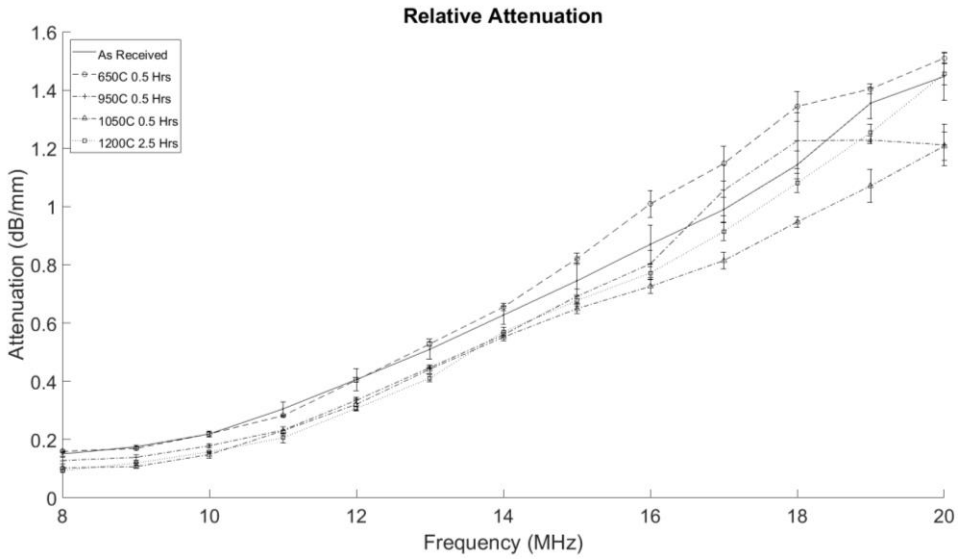

Figure 21: Attenuation measurements of 316L PBF at all material states

Note, the lower bounds of the x-axis in Figure 19 through Figure 21 are 8 MHz which is nearly twice the highest operating frequency (4.2 MHz) in the NLU measurement. As the attenuation of each sample tends to converge at low frequencies, the effects of attenuation differences on the relative NLU measurements are minimal.

5.7 Recrystallized Results

The final heat treatment for each sample was intended to fully recrystallize the material and explore if any residual microstructural features are detectible with the nonlinear ultrasonic techniques. The high temperature and long holding time for this heat treatment caused significant changes in each of the measurement techniques and are presented separately in this section.

5.7.1 Nonlinear Ultrasound Recrystallized

Only NLU measurements for the AM specimens were able to be made, likely caused by a large increase in attenuation that is additionally discussed in Section 5.7.6. The

high attenuation in the wrought specimens inhibited the detection of A_2. For both AM specimens, the relative β value increased significantly. As β is sensitive to many things, the cause of this increase is better examined with the wide range of other characterization techniques.

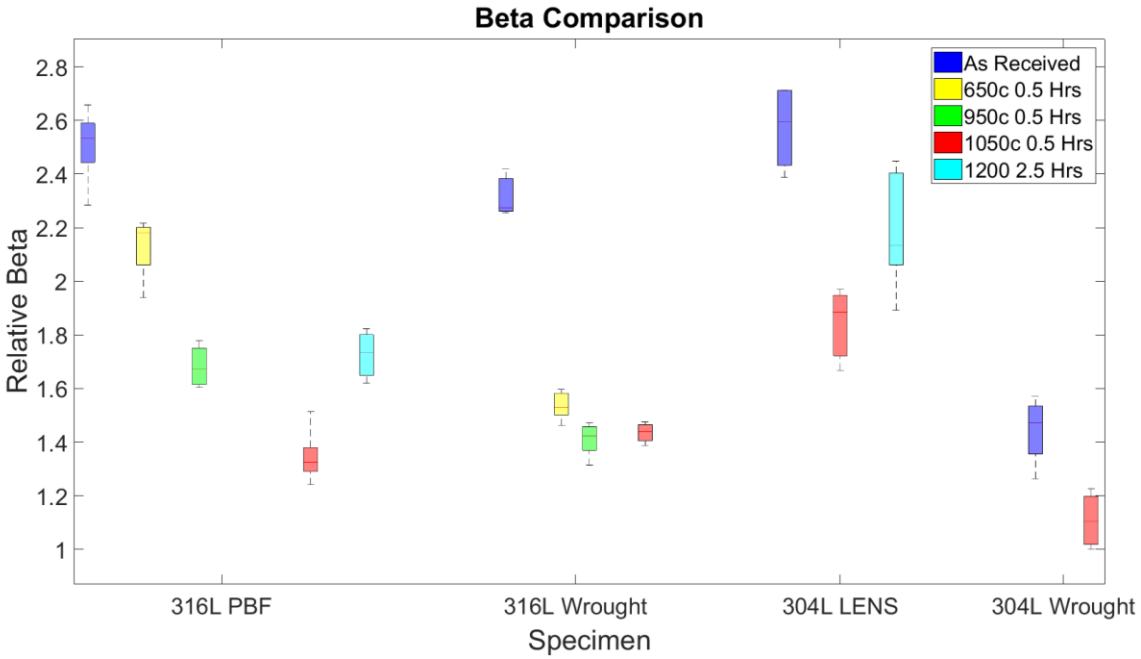

Figure 22: An updated box plot chart comparing normalized β values and includes values for the recrystallization heat treatment.

5.7.2 Hardness Recrystallized

Hardness continues to decrease in all four samples after the final heat treatment. Therefore, the high correlation seen in Figure 15 is decreased when the recrystallized point is included in Figure 23. The divergence in trends between these two metrics shows that β is sensitive to different metrics than hardness.

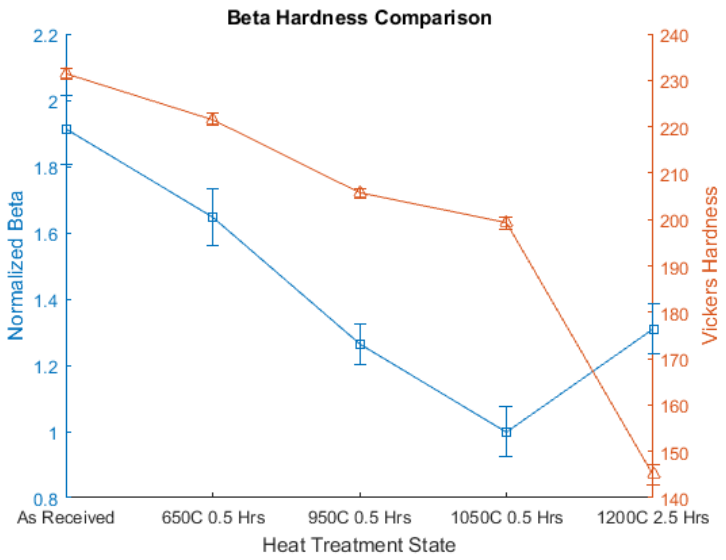

Figure 23: An updated graph of 316L PBF hardness/Beta comparison that now includes the recrystallized state.

5.7.3 EBSD Recrystallized

Figure 16 includes the IPF-z for all heat treatment steps for 316L PBF including the final heat treatment. These images confirm the suspicion that the microstructure of this specimen has undergone a radical change during the final heat treatment that corresponds to a large amount of recrystallization.

In Figure 25, Reference Orientation Deviation (ROD) mapping can be used to show that the recrystallization does not appear to be complete at 1200°C. However, the recrystallization that has occurred has had a significant impact on the microstructure. ROD maps are made by comparing a grain's orientation measurement with an associated referenced orientation [47]. The non-recrystallized grains are multicolored in Figure 25, whereas solid colored grains indicate recrystallization has occurred. The solid red grains are an artifact of poor grain thresholding when determining neighboring grain orientation. These maps were made by Philip Noell at Sandia National Labs for this study. Figure 24

and Figure 25 are taken from EBSD images done with a larger step size than shown in Figure 16.

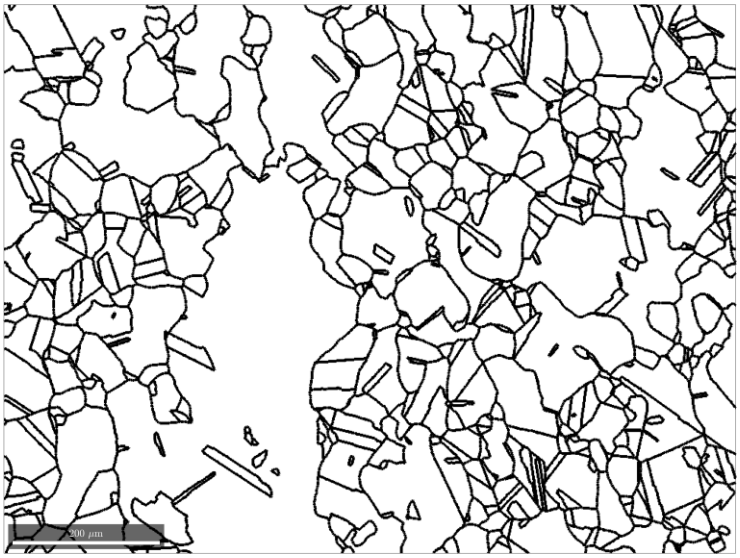

Figure 24: A grain map of the 316L PBF sample after 1200°C

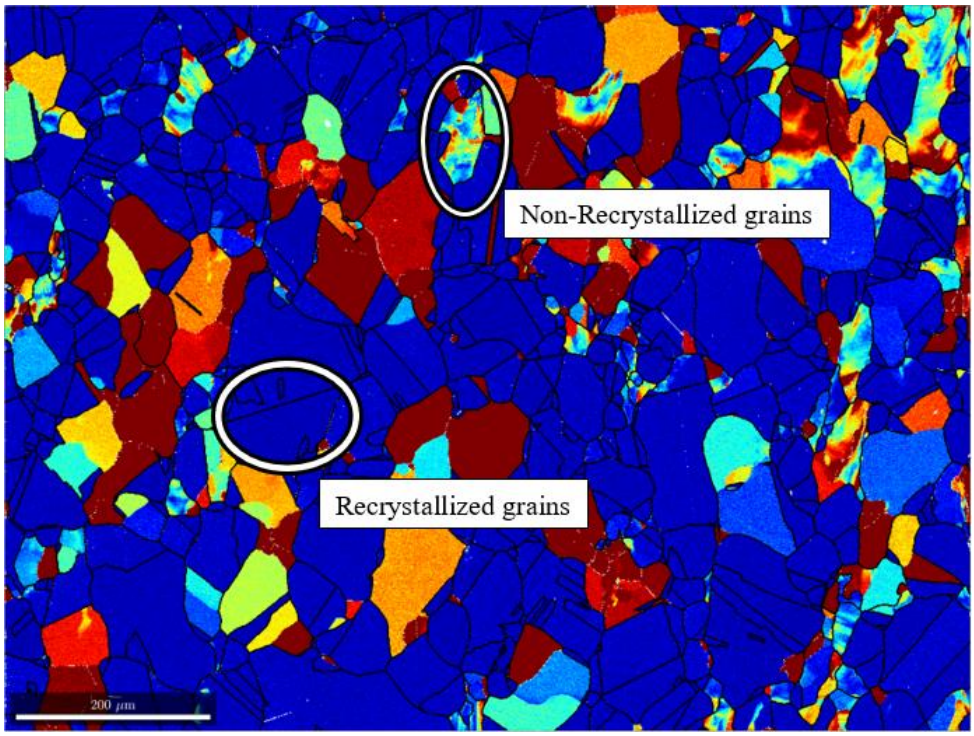

Figure 25: 316L PBF Recrystallized Reference Orientation Deviation (ROD) Map

5.7.4 GND Recrystallized

Large deviations in the relationship between β and GND density for the 316L PBF specimen comes at the final heat treatment at 1200$^{\circ C}$ as seen in Figure 26.

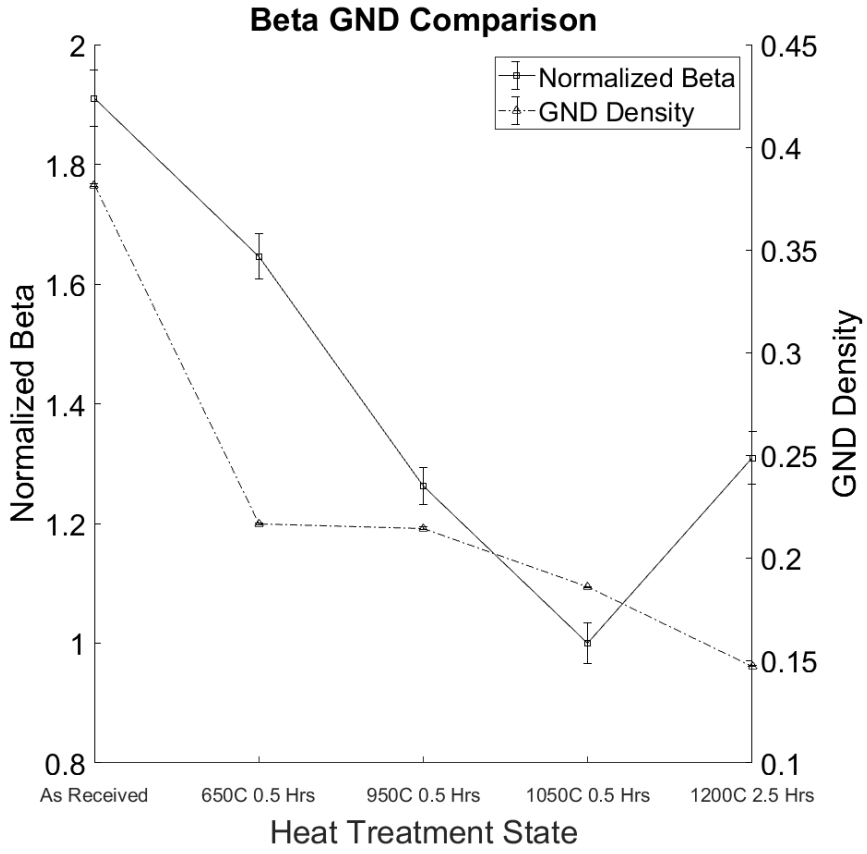

Figure 26: Updated mean GND density and β plotted concurrently of 316L PBF with recrystallization point

Diverging from the previous trend, β increases by 10.85% after the final heat treatment despite a continued decrease in GND density by 20.69%. The correlation coefficient for these two variables across both recrystallized and non-recrystallized regimes is reduced to 0.8155, when results from the recrystallized state are included. The continued decrease of GND density was expected after recrystallization but its divergence with β shows that new sources of acoustic nonlinearity causing an increase in β.

5.7.5 Texture Recrystallized

Large microstructural change caused by recrystallization can also be seen in Figure 27, which shows the change in crystalline texture between the first and last heat treatment states. The grain orientation begins at 650°C with a strong 100 fiber that then develops to show a strong 110 texture and other variations in the 1200°C specimen. Since the β calculated here is a relative measure of second harmonic generation, it is difficult to make absolute statements about the impact of the large microstructural changes caused by recrystallization on β.

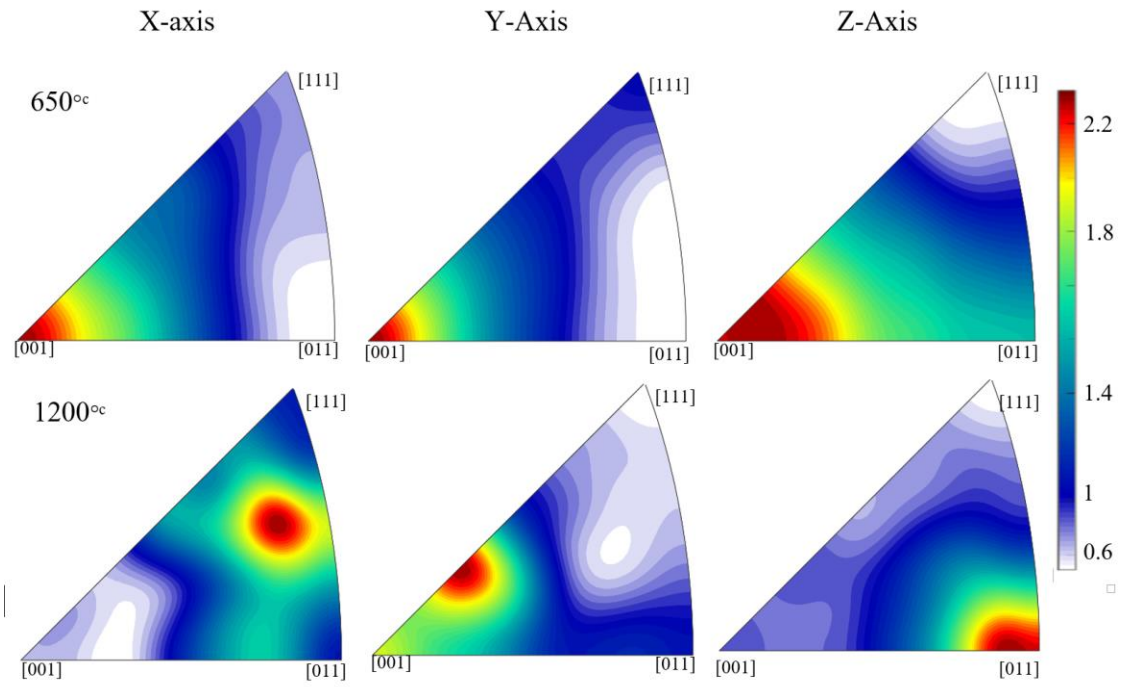

Figure 27: Texture analysis of 316L PBF after first (top row) and last (bottom row) heat treatments

5.7.6 Attenuation Recrystallized

As mentioned in Section 5.7.1, NLU measurements could not be made with the wrought specimens. The attenuation of 316L PBF and 316L Wrought are compared before and after heat treatment in Figure 28.

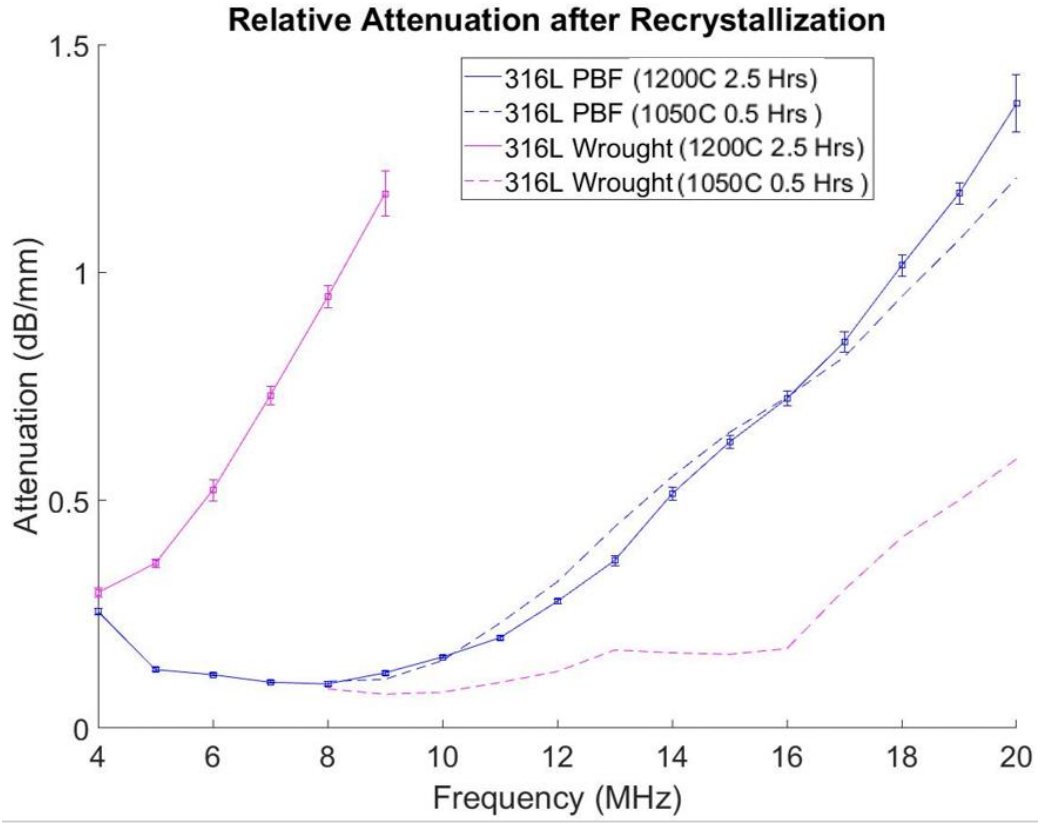

Figure 28: Attenuation of both 316L samples after recrystallization

The low frequency attenuation values are difficult to produce with this experimental setup as it begins to near the lower end of the transducer bandwidth and the separation of the two amplitudes (described in Figure 12) is greatly reduced. Throughout the frequency range, there is a large increase in attenuation before and after the final heat treatment of the 316L Wrought specimen that is not seen with the 316L PBF sample. This increase in

attenuation contributed to the inability to make NLU measurements with the current setup for the wrought specimens at this final heat treatment state.

CHAPTER 6. CONCLUSION AND FUTURE WORKS

6.1 Conclusion

This research shows the sensitivity of the nonlinear acoustic parameter, β to changes in the microstructure of additively manufactured metals. The different trends in measured β between the 316L PBF and 316L Wrought specimens follow the expected microstructural changes from previous literature comparisons between AM and traditional manufactured specimens. Quantitative measures of geometrically necessary dislocations show that the heat treatment profile is effective in reducing the number of dislocations. The statistical correlation between β and GND density is strong, but β is not uniquely sensitive to dislocations as other microstructural features influence acoustic nonlinearity.

On the other hand, β appears to have an excellent correlation with hardness of the material. Note that hardness is a macroscopic consequence of the dislocations as well as other features (grain boundaries) in the microstructure. A multiphysics approach to the qualification of AM parts would provide multiple facets of understanding and insurance of a printed part before it is used in critical scenarios. NLU can provide useful information of the microstructure and can act as a comparative measure between specimens.

6.1.1 Recrystallized Case

The trend between β and GND density diverges following large-scale recrystallization. The final heat treatment associated with recrystallization was initially proposed in this work for exploratory purposes and to see if any remaining information could be detected with NLU. When large amounts of recrystallization occur, the relative

changes tracked with β are lost in the parameter's reaction to a new microstructure. Evidence of significant recrystallization is seen from EBSD measurements and resulting analysis of grain structure. Expectedly, the GND density continued to decrease after large scale recrystallization. The exact contributions to the increase of β after recrystallization are currently unknown and provide a new avenue for discovery.

6.2 Future Works

Future works stemming from this thesis include the continuation of studying NLU sensitivity in AM and include larger scale implementations of NLU to the qualification of AM. Perinate to the continuation of this work, a study can be made of β and its response to anisotropy in AM materials could be made. AM samples could be printed with intentional anisotropic properties and microstructure. By orienting the build correctly, a Rayleigh wave setup would be able to interact with the different microstructural regions to determine how β would react. This could also show how different printing parameters are detectible with β and its usefulness in comparing printed parts to ensure the consistency of a printer.

On a larger scale, the implementation of NLU to AM qualification would require significant work. *In situ* process monitoring with NLU would allow for real time feedback between the printer and the part being printed. This would allow a print to be assessed before it is complete to determine if a printing parameter needs adjustment or if the print should be abandoned before wasting valuable machining time and cost. The experimental setup used in this work would not be feasible in a process monitoring setup. Possible options include setups involving laser based harmonic generation and detection [48] or setups involving ultrasonic generation imbedded in the printer.

REFERENCES

[1] Yang L, Hsu K, Baughman B, Godfrey D, Medina F, Menon M, et al. Additive Manufacturing of Metals: The Technology, Materials, Design and Production. Springer International Publishing; 2017. https://doi.org/10.1007/978-3-319-55128-9.

[2] Waller JM, Saulsberry RL, Parker BH, Hodges KL, Burke ER, Taminger KM. Summary of NDE of additive manufacturing efforts in NASA, Boise, Idaho: 2015, p. 51–62. https://doi.org/10.1063/1.4914594.

[3] Seifi M, Salem A, Beuth J, Harrysson O, Lewandowski JJ. Overview of Materials Qualification Needs for Metal Additive Manufacturing. JOM 2016;68:747–64. https://doi.org/10.1007/s11837-015-1810-0.

[4] Gouge M, Michaleris P. Chapter 1 - An Introduction to Additive Manufacturing Processes and Their Modeling Challenges. In: Gouge M, Michaleris P, editors. Thermo-Mechanical Modeling of Additive Manufacturing, Butterworth-Heinemann; 2018, p. 3–18. https://doi.org/10.1016/B978-0-12-811820-7.00002-1.

[5] Beese AM. Chapter 5 - Microstructure and Mechanical Properties of AM Builds. In: Gouge M, Michaleris P, editors. Thermo-Mechanical Modeling of Additive Manufacturing, Butterworth-Heinemann; 2018, p. 81–92. https://doi.org/10.1016/B978-0-12-811820-7.00007-0.

[6] Wright SI, Nowell MM, Field DP. A Review of Strain Analysis Using Electron Backscatter Diffraction. Microscopy and Microanalysis 2011;17:316–29. https://doi.org/10.1017/S1431927611000055.

[7] Gorsse S, Hutchinson C, Goune M, Banerjee R. Additive manufacturing of metals: a brief review of the characteristic microstructures and properties of steels, Ti-6Al-4V and high-entropy alloys. vol. 18. 2017.

[8] Matlack KH, Kim J-Y, Jacobs LJ, Qu J. Review of Second Harmonic Generation Measurement Techniques for Material State Determination in Metals. Journal of Nondestructive Evaluation 2014;34:273. https://doi.org/10.1007/s10921-014-0273-5.

[9] Energetics Incorporated. Measurement Science Roadmap for Metal-Based Additive Manufacturing, Columbia, Maryland: National Institute of Standards and Technology; 2013.

[10] Mix P. Introduction to Nondestructive Testing : A Training Guide. 2nd ed. Wiley; 2005.

[11] Akira Hikata, Bruce B. Chick, Charles Elbaum. Dislocation Contribution to the Second Harmonic Generation of Ultrasonic Waves. Journal of Applied Physics 1965;36:229–36. https://doi.org/10.1063/1.1713881.

[12] Kim J-Y, Jacobs LJ, Qu J, Littles JW. Experimental characterization of fatigue damage in a nickel-base superalloy using nonlinear ultrasonic waves. The Journal of the Acoustical Society of America 2006;120:1266–73. https://doi.org/10.1121/1.2221557.

[13] Cantrell JH, Zhang X-G. Nonlinear acoustic response from precipitate-matrix misfit in a dislocation network. Journal of Applied Physics 1998;84:5469–72. https://doi.org/10.1063/1.368309.

[14] Ruiz A, Ortiz N, Medina A, Kim J-Y, Jacobs LJ. Application of ultrasonic methods for early detection of thermal damage in 2205 duplex stainless steel. NDT & E International n.d.;54:19–26.

[15] Viktorov IA. Rayleigh and Lamb Waves: Physical Theory and Applications. Springer US; 1967.

[16] Jones S. Ground vibration from underground railways: how simplifying assumptions limit prediction accuracy 2010.

[17] Hamilton MF, Blackstock DT. Nonlinear Acoustics. Academic Press; 1998.

[18] Jan Herrmann, Jin-Yeon Kim, Laurence J. Jacobs, Jianmin Qu, Jerrol W. Littles, Michael F. Savage. Assessment of material damage in a nickel-base superalloy using nonlinear Rayleigh surface waves. Journal of Applied Physics 2006;99:124913. https://doi.org/10.1063/1.2204807.

[19] Thompson SM, Bian L, Shamsaei N, Yadollahi A. An overview of Direct Laser Deposition for additive manufacturing; Part I: Transport phenomena, modeling and diagnostics. Additive Manufacturing 2015;8:36–62. https://doi.org/10.1016/j.addma.2015.07.001.

[20] Smith RL. Ultrasonic materials characterization. NDT International 1987;20:43–8. https://doi.org/10.1016/0308-9126(87)90371-3.

[21] Smith RL. The effect of grain size distribution on the frequency dependence of the ultrasonic attenuation in polycrystalline materials. Ultrasonics 1982;20:211–4. https://doi.org/10.1016/0041-624X(82)90021-X.

[22] Treiber M, Kim J-Y, Jacobs LJ, Qu J. Correction for partial reflection in ultrasonic attenuation measurements using contact transducers. The Journal of the Acoustical Society of America 2009;125:2946–53. https://doi.org/10.1121/1.3106125.

[23] Rogers PH, Van Buren AL. An exact expression for the Lommel-diffraction correction integral. The Journal of the Acoustical Society of America 1974;55:724–8. https://doi.org/10.1121/1.1914589.

[24] Zeitvogel DT, Matlack KH, Kim J-Y, Jacobs LJ, Singh PM, Qu J. Characterization of stress corrosion cracking in carbon steel using nonlinear Rayleigh surface waves. NDT & E International 2014;62:144–52. https://doi.org/10.1016/j.ndteint.2013.12.005.

[25] Media R. Classes of Stainless Steel. Metal Supermarkets - Steel, Aluminum, Stainless, Hot-Rolled, Cold-Rolled, Alloy, Carbon, Galvanized, Brass, Bronze, Copper 2015. https://www.metalsupermarkets.com/classes-of-stainless-steel/ (accessed April 12, 2020).

[26] Rokosz K, Lahtinen J, Hryniewicz T, Rzadkiewicz S. XPS depth profiling analysis of passive surface layers formed on austenitic AISI 304L and AISI 316L SS after high-current-density electropolishing. Surface and Coatings Technology 2015;276:516–20. https://doi.org/10.1016/j.surfcoat.2015.06.022.

[27] Design Guidelines for the Selection and Use of Stainless Steel. Specialty Steel Industry of the United States; 1993.

[28] Raj B, Mudali K, Vijayalakshmi M, Mathew MD, Bhaduri AK, P.Chellapandi, et al. Development of Stainless Steels in Nuclear Industry: With Emphasis on Sodium Cooled Fast Spectrum Reactors History, Technology and Foresight. Advanced Materials Research 2013;794:3–25. https://doi.org/10.4028/www.scientific.net/AMR.794.3.

[29] Garlea E, Choo H, Sluss CC, Koehler MR, Bridges RL, Xiao X, et al. Variation of elastic mechanical properties with texture, porosity, and defect characteristics in laser powder bed fusion 316L stainless steel. Materials Science and Engineering: A 2019;763:138032. https://doi.org/10.1016/j.msea.2019.138032.

[30] Jacob G, Brown CU, Donmez MA, Watson SS, Slotwinski J. Effects of powder recycling on stainless steel powder and built material properties in metal powder bed fusion processes. Gaithersburg, MD: National Institute of Standards and Technology; 2017. https://doi.org/10.6028/NIST.AMS.100-6.

[31] Horiba Instruments, INC. A Guidebook to Particle Size Analysis. Irvince, CA: 2017.

[32] Kim G, In C-W, Kim J-Y, Kurtis KE, Jacobs LJ. Air-coupled detection of nonlinear Rayleigh surface waves in concrete—Application to microcracking detection. NDT & E International 2014;67:64–70. https://doi.org/10.1016/j.ndteint.2014.07.004.

[33] Smith TR, Sugar JD, Schoenung JM, San Marchi C. Anomalous Annealing Response of Directed Energy Deposited Type 304L Austenitic Stainless Steel. JOM 2018;70:358–63. https://doi.org/10.1007/s11837-017-2711-1.

[34] Susan DF, Kammler D, Rodriguez MA, Michael JR, Ghanbari Z, Jared BH, et al. The Effects of Annealing Treatments on AM 316L Stainless Steel. Sandia National Lab. (SNL-NM), Albuquerque, NM (United States); 2018.

[35] Torello D, Thiele S, Matlack KH, Kim J-Y, Qu J, Jacobs LJ. Diffraction, attenuation, and source corrections for nonlinear Rayleigh wave ultrasonic measurements. Ultrasonics 2015;56:417–26. https://doi.org/10.1016/j.ultras.2014.09.008.

[36] Thiele S, Kim JY, Qu J, Jacobs LJ. Air-coupled detection of nonlinear Rayleigh surface waves to assess material nonlinearity. Ultrasonics 2014;54:1470–5. https://doi.org/10.1016/j.ultras.2014.04.020.

[37] ASTM International. ASTM E92-17, Standard Test Methods for Vickers Hardness and Knoop Hardness of Metallic Materials 2017.

[38] Nowell M, Witt R, True B. EBSD Sample Preparation: Techniques, Tips, and Tricks. Microscopy Today 2005;July:44. https://doi.org/10.1017/S143192760550672X.

[39] Bachmann F, Hielscher R, Schaeben H. Texture Analysis with MTEX – Free and Open Source Software Toolbox. Solid State Phenomena 2010. /SSP.160.63 (accessed April 10, 2020).

[40] Gao H, Huang ying-sheng. Geometrically necessary dislocation and size-dependent plasticity. Scripta Materialia, v48, 113-118 (2003) 2003;48. https://doi.org/10.1016/S1359-6462(02)00329-9.

[41] Arsenlis A, Parks DM. Crystallographic aspects of geometrically-necessary and statistically-stored dislocation density. Acta Materialia 1999;47:1597–611. https://doi.org/10.1016/S1359-6454(99)00020-8.

[42] Brewer LN, Field DP, Merriman CC. Mapping and Assessing Plastic Deformation Using EBSD. In: Schwartz AJ, Kumar M, Adams BL, Field DP, editors. Electron Backscatter Diffraction in Materials Science, Boston, MA: Springer US; 2009, p. 251–62. https://doi.org/10.1007/978-0-387-88136-2_18.

[43] Pantleon W. Resolving the geometrically necessary dislocation content by conventional electron backscattering diffraction. SCRIPTA MATER 2008;58:994–7. https://doi.org/10.1016/j.scriptamat.2008.01.050.

[44] Fressengeas C, Beausir B, Kerisit C, Helbert A-L, Baudin T, Brisset F, et al. On the evaluation of dislocation densities in pure tantalum from EBSD orientation data. Matériaux & Techniques 2019;106:14. https://doi.org/10.1051/mattech/2018058.

[45] Wan T, Naoe T, Wakui T, Futakawa M, Obayashi H, Sasa T. Effects of Grain Size on Ultrasonic Attenuation in Type 316L Stainless Steel. Materials (Basel) 2017;10. https://doi.org/10.3390/ma10070753.

[46] Van Pamel A, Nagy PB, Lowe MJS. On the dimensionality of elastic wave scattering within heterogeneous media. The Journal of the Acoustical Society of America 2016;140:4360–6. https://doi.org/10.1121/1.4971383.

[47] Buchheit TE, Carroll JD, Clark BG, Boyce BL. Evaluating Deformation-Induced Grain Orientation Change in a Polycrystal During In Situ Tensile Deformation using EBSD. Microscopy and Microanalysis 2015;21:969–84. https://doi.org/10.1017/S1431927615000677.

[48] Herrmann J, Jacobs LJ, Qu J, Kim J. Generation and Detection of Higher Harmonics in Rayleigh Waves Using Laser Ultrasound. AIP Conference Proceedings 2006;820:262–9. https://doi.org/10.1063/1.2184538.